GEAR FAULT DETECTION USING NON-CONTACT MAGNETIC ROTATION POSITION SENSORS

by

Michael Taylor

A thesis submitted to the Department of Mechanical Engineering

In conformity with the requirements for

the degree of Masters of Applied Science

Queen's University

Kingston, Ontario, Canada

(October, 2010)

Abstract

This thesis is an investigation of possible applications for a low cost non-contact magnetic rotational position sensor. A single stage gearbox operating spur gears was instrumented with these sensors along with typical optical encoders. These rotational position devices were used independently to measure gearbox Transmission Error (TE) during operation. Basic filtering techniques were used to condition the TE so that localized faults were observable. Characteristic feature extraction on the TE using RMS, Kurtosis and Crest Factor was used to quantify gearbox dynamics. These features were able to measure dynamic changes in gearbox health, such as wearing in the gears or the progression of a fault resulting in full tooth failure. These sensor attributes are ideal for machine condition monitoring applications where catastrophic failure can be forewarned by incipient fault detection.

Co-Authorship

This thesis was solely written by the author, Michael Taylor.

Based on research contained in this thesis, the following papers for conferences were written with co-authorship by my co-supervisors:

Taylor, M, M Timusk, and CK Mechefske, Gear Fault Detection under Variable Speed and Load Conditions using Transmission Error Measurements, *Condition Monitoring and Diagnostic Engineering Management - COMADEM 2010*, Nara, Japan, 28 June – 2 July 2010

Taylor, M, M Timusk & CK Mechefske, Fault Detection in Gear Boxes using a Non-Contact Rotational Position Sensor, *The Fifth International Conference on Condition Monitoring and Machinery Failure Prevention Technologies*, Edinburgh, Scotland, 15-18 July 2008.)

Acknowledgements

I would like to thank my supervisor, Dr. Chris Mechefske for his guidance, patience, and humor throughout my research here. During times when results were discouraging, his enthusiasm and encouraging words motivated me. In the end, our determination prevailed.

My thanks are also deserved by my co-supervisor, Dr. Markus Timusk for his wisdom and direction that laid the foundation of results for this research.

I would also like to recognize and express gratitude for funding and support received from the Natural Sciences and Engineering Research Council of Canada (NSERC), Litens Automotive Group, and MITACS.

These results would not have been possible to obtain without the expertise of the McLaughlin Hall machine shop staff, so I am grateful for their precision of their efforts.

Finally, and most importantly, I would like to thank my family, for their love and support in all my endeavors.

Table of Contents

List of Figures

Nomenclature

The following abbreviations and acronyms are used in this thesis. They are defined here as a quick reference.

SDRG	System Dynamics Research Group
TE	Transmission Error
FFT	Fast Fourier transform
V DC	Volts (Direct Current)
V AC	Volts (Alternating Current)
CAD	Computer aided design
NI	National Instruments
CNC	Computer numerically controlled
ABS	Acrylonitrile butadiene styrene (plastic)
RMS	Root Mean Square

Chapter 1

Introduction

1.1 Project Inception

The System Dynamics Research Group (SDRG) in the Department of Mechanical and Materials Engineering at Queen's University was approached by an automotive part developer/manufacturer with a new type of rotational position encoder. The goal of the collaboration was to evaluate sensor performance and determine potential future applications.

1.2 Project Background - Maintenance Strategies

Approximately half of all operating costs in most processing and manufacturing operations can be attributed to maintenance. This provides significant motivation to develop strategies to minimize these costs. In many cases, it is acceptable to run equipment until failure (breakdown maintenance) if failure modes are safe, inexpensive, and the process is interruptible. In other situations, there may be sufficient statistical data which predicts machine wear as a function of load and speed, allowing scheduled downtimes (preventive maintenance) to repair or replace worn items. This method is preferred if replacement/repair costs are low, unexpected shutdowns expensive, and scheduled interruptions acceptable. In almost all cases of failure in heavily loaded machinery, there is some system degradation (incipient failure) prior to catastrophic failure. Condition based monitoring is utilized in cases where replacement parts and interruption to production are expensive, failure modes are costly or dangerous, and methods exist to accurately detect, diagnose and/or predict a failure. Many examples of such cases exist in the mining and mineral processing industries where there are extremely large custom machinery operating around the clock[1].

1.3 Selection of Project Application

Building on SDRG's expertise and equipment on site, sensor evaluation with a gearbox was selected. This was an appropriate choice as there are several different ways in which gearboxes exhibit incipient failure. Each failure is likely to result in variations in relative shaft rotational position as a function of time.

1.4 Statement of Objective

This thesis will examine the ability of a non-contact magnetic rotational position sensor to allow detection and diagnosis of gearbox deterioration.

1.5 Organization of Thesis

Chapter One is a brief introduction to the project. It clarifies motivation for a study into these sensors and the discovery of new applications. Chapter Two is a full literature review, conducted to examine failure modes of gearboxes, past work in gearbox fault detection, and other types of rotational position sensors. Chapter Three details the characteristics and basic signal processing of the non-contact magnetic sensor to obtain rotational position. Chapter Four includes a full description of the apparatus used, including the gearbox, spur gears used, and the faults introduced to the gears. Chapter Five shows all the results of the testing carried out. Chapter Six presents a full discussion of the results outlined in Chapter Five. Chapter Seven provides the conclusions and recommendations for future work on this topic.

Chapter 2

Literature Review

2.1 Introduction

This chapter provides readers with a basic understanding of spur gear design. The concept of transmission error is then introduced. The basic modes of gear failure are discussed briefly. Current gear train fault detection techniques are then reviewed to provide a background. The methods most commonly used in industry are highlighted. Finally, an assessment of current rotational displacement sensors outlines the alternatives for the sensor used in this study (and described in detail in Chapter 3).

2.2 Spur Gears

Direct power transmission from the motive source to a load is not always possible to achieve. Design requirements such as space restrictions, part orientation, velocity reductions, and torque multiplication make it often necessary to translate and transmit the power via a gear train. The simplest form of gear train is a parallel shaft gearbox using spur gears.

Spur gear teeth are most commonly cut to have an involute curve, which is a shaped load bearing surface. This shape was evaluated by de la Hire in 1694, and confirmed by Leonard Euler (demonstrating mathematically the superiority of the involute shape)[2]. Other variations such as the Wildhaber-Novikov and Vickers-Bostock-Bramley will not be discussed in this report as they are not being used. In spur gears, tooth flanks run parallel to the shaft axes, and do not impart any axial force on the gear. During operation, the number of teeth actually meshing at any given instant fluctuates. This occurs because a tooth beginning to 'engage' a mating tooth is not necessarily synchronous to a tooth 'finishing' a mesh. This leads to varying stresses and deflections in the teeth, which result in non-uniform force transmission of the mating gears[3]. Some strategies such as root relief or end relief (change of tooth profile at root and/or tip) are employed to reduce this effect.

It is important that gears be run at design load, or else increased variations in load distribution between teeth can occur[4]. This type of error is understandably termed 'Transmission Error' (TE)[5]. Classic work on this subject was carried out by Gregory, Harris and Munro in the late 1950's.

2.3 Transmission Error

A definition of Transmission Error, according to Smith[15] is

> ***"...TE, and is defined as the difference between the position that the output shaft of a gear drive would be if the gearbox were perfect, without errors or deflections, and the actual position of the output shaft. It may be expressed either as an angular displacement from the 'correct' position or sometimes more conveniently as a linear displacement along a line of action, i.e., at the base circle radius or as a linear displacement at pitch circle radius."***

Similarly, consider an input shaft rotating at an absolutely steady angular velocity. For perfectly involute gears operating at design load, the output velocity would be identical. This is not the case in practice as production involutes are not perfect and gear loading varies. TE can be measured as the difference in position of the actual output shaft displacement with respect to the theoretical displacement[4]. This small error will cause gears to vibrate. A typical TE trace is found in Figure 2.1.

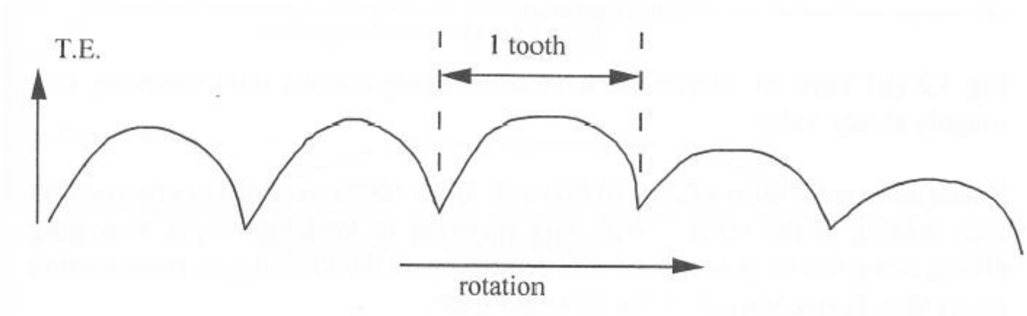

Figure 2.1 - Typical section of TE for spur gears.

2.4 Gear Failure

Gears undergo two main types of stress when loaded. The contact load on the face of the gear generates a large contact stress on the face, as well as creating a bending moment which leads to flexion of the tooth and root stress. Gear deterioration and failure typically occurs by one of these two mechanisms.

The most common failure mode of gears is tooth wear. The initial wear process, known as "run in", removes high spots and surface deformities, resulting in a polished surface. This is not usually a concern, as the material removal rate drops off once equilibrium has been attained and the wear particles generated are removed by the oil filter.

The next location of tooth wear is generally on the tooth surface near the tip or root due to sliding motion during operation. Material removal due to sliding should not occur at the pitch diameter as the teeth are not sliding relative to each other at these points, but rotating.

Pitting resulting from surface fatigue can be a concern depending on where it is located. Since there is no sliding motion at the pitch line, high spots will create localized stress concentrations, which cause fatigue and pit formation. Pitting occurring at other locations on the tooth face can indicate misalignment or overload conditions depending on the distribution across the face width. Gear tooth fracture can also result due to fatigue failure. Such cases can be brought on by foreign particles interfering with the mesh, causing extremely high point stresses[3].

2.5 Current Fault Detection Techniques

2.5.1 Introduction

The two predominant condition based monitoring techniques used with gear boxes today are oil and vibration analysis. These methods have proven to be effective in certain situations for health analysis of gear boxes. This section is intended to discuss the abilities and limitations of these two systems and the inherent value of early fault detection in industries where machine downtime is expensive and/or dangerous.

2.5.2 Oil and Wear Particle Analysis

There are a wide variety of oil and wear particle analysis techniques. Methods not relevant to the detection of failure in gearboxes will be omitted from this review. Oil and wear particle analysis with respect to condition monitoring of gearboxes is primarily off-line, where samples must be taken and analyzed (usually off-site).

2.5.2.1 Spectrographic Methods

Spectrographic methods determine the presence of metallic particles within gearbox oil by observing different light emissions when subjected to an excitation. Excitation methods range from subjecting the sample to open flame, X-ray (gamma ray), infrared, and laser beams. Spectrography can give both qualitative (what type of metals) and quantitative results with respect to particulates present, which are used to detect and diagnose wear of the respective components.

2.5.2.2 Ferrography

Ferrography quantifies the amount of large and small ferrous particles in a sample. Direct reading ferrography is an automated method, sorting oil particles into large and small by applying a magnetic field over a flow of oil. By measuring the amount of light blocked by particulates, the number of particles is quantified and compared. Analytical ferrography on the other hand allows an experienced technician to identify different wear particles by type and assess the cause of the wear. This method involves analysing samples under a microscope and is much more costly than direct reading.

2.5.2.3 Magnetic Chip Detectors

Magnetic chip detectors are similar to ferrography in that only ferromagnetic particles are collected and examined. A magnetic plug is placed upstream of the filtration device, attracting magnetic particles. A higher frequency of large particles indicates imminent gear failure. Statistical means are usually adopted for particle counting to save time and money. Flow rate decay as the oil passes through different porosity membranes will give a general picture of particle size distribution as well as quantity. A more commonly used method is light blockage using a laser and a detector to measure size and quantities of particles. Image analysis using computer vision calculates size, shape, and amount of particles present, but errors can occur when many small particles clump together[6].

2.5.2.4 LaserNet Fines

Magnetic chip detectors are similar to ferrography in that only ferromagnetic particles are collected and examined. A magnetic plug is placed upstream of the filtration device, attracting magnetic particles. A higher frequency of large particles indicates imminent gear failure. Statistical means are usually adopted for particle counting to save time and money. Flow rate decay as the oil passes through different porosity membranes will give a general picture of particle size distribution as well as quantity. A more commonly used method is light blockage using a laser and a detector to measure size and quantities of particles. Image analysis using computer vision calculates size, shape, and amount of particles present, but errors can occur when many small particles clump together[6].

2.5.2.5 Oil and Wear Particle Analysis Conclusion

Oil and wear particle analysis (generally) cannot predict failure in real-time and is usually performed offsite. This limits the number of applications where it is a viable condition monitoring technique. It is a suitable analysis method able to detect incipient failure provided failure occurs in a slow predictable manner[7].

2.5.3 Vibration Methods

Vibration methods have been the primary means of gear fault detection for quite some time, with a wide array of analysis methods employed. Although the proposed condition monitoring method does not measure vibration directly, this section is included to show past work, and highlight signal analysis methods which may be applied to the rotational position signal.

In order to collect vibration data, an appropriate sensor must be selected. There are three basic types of transducers: displacement, velocity, and acceleration. Displacement transducers are either contact (LVDT) or non-contact (Eddy Current or Laser Vibrometer). Velocity transducers are piezoelectric or electromechanical, and accelerometers are usually piezoelectric. Due to the higher range of frequencies in the vibrations expected in gearboxes and the relatively high vibration amplitudes, accelerometers are usually chosen to maximize relative amplitude response.

Piezoelectric accelerometers are fully contacting probes which mount rigidly on bearings or machine casings in such a way that the transmission path from vibration source to the measurement point is minimized. When the sensor moves relative to an inertial mass within, a stress change on the piezoelectric crystal causes an electric output proportional to force. Vibration data can be collected in a few different manners, such as a bump test while the gearbox is inert to determine the transfer function of the casing, or during run up/down transient operation. Steady state uniform time sampling is the most common type of vibration measurement.

There are many naturally occurring vibrations in gearboxes. Uniformly occurring events such as tooth deflection under load, wear, and gear design errors appear at the tooth meshing frequency. As discussed previously, flank wear due to the sliding motion between teeth causes material removal at two locations on the tooth flank, which give rise to the second harmonic of tooth meshing frequency. Eccentricity and bent shaft result in large low frequency harmonics, as well as adding sidebands to the tooth mesh frequency. Randomly spaced defects, including root cracking and localized pitting give a wide range of harmonics and sidebands throughout the frequency spectrum[8].

2.6 Rotational Position Displacement Devices

2.6.1 Incremental Encoders

Rotational position sensors are of particular importance to this project. Traditional optical encoders use photointerrupters to convert rotational motion into electrical pulses. Using a stationary mask with uniformly distributed slots and a rotating codewheel that is configured in the same manner, the photodetector is alternately blocked and unblocked from the light source. It is important that there be two sets of sensing units spaced one quarter of an increment out of phase to determine the direction of rotation. By keeping track of conditions as pulses rise or fall, rotational position can be determined. Encoder specification sheets indicate that, for example, a 360 pulse encoder can be used in either 1X, 2X, and 4X resolution modes. 4X means that the rising and falling of pulses for the two channels are monitored, therefore the 360 pulse encoder actually has 1440 count/revolution resolution[9]. Other means of sensing binary regions have been developed using conductive materials for radial lines and a contacting sensor.

2.6.2 Interference Fringe Encoders

Interference fringe encoders use moiré patterns to further increase accuracy. The moiré effect occurs when the straight slotted stationary mask is used in conjunction with a codewheel that has angled slots. Light emitter-detection pairs yield sinusoidal signals, which, when coupled with a one quarter out of phase signal, can be interpolated to a much higher resolution than the optical grating[2].

It is important to recognize the shortcomings of incremental encoders. They typically have a third channel to index the position to a ‘home position’. This means that they have no sense of absolute position when turned on, and must rotate past the index to achieve this. Also, if interference disguises a pulse momentarily, the position is lost until the index pulse is reached. Optical encoders are sensitive to shock and vibration, which can either shatter the slotted disk or vibrate it so that pulses are missed. Furthermore, dust particle buildup inside the transducers can create problems in optical systems.

2.6.3 Absolute Position Encoders

Absolute position encoders on the other hand have unique digital outputs representing a position. The inner disk is comprised of several concentric rings, each with its own reading system. Each reading system will report either 1 or 0, thus the encoder has a resolution of 2^n, where n is the number of concentric rings. Absolute encoders have been made with natural binary numbers representing consecutive positions, however a more common convention is to use Gray code to avoid errors when switching many bits at the same time (ie 0111 to 1000).

Absolute encoders have resolution ranges from 6 to 21 bits, although 8-12 are most common, which corresponds to 256-4,096 counts in a revolution. They are primarily used in relatively slow moving applications where absolute position is important (robotics). Since they use optical means to read each track, they are subject to similar constraints with respect to shock, vibration, and environment. Incremental encoders provide higher resolutions (up to 81,000 counts/revolution) at lower costs, and are the most common type of encoder.

2.6.4 Hall Effect Sensor

A simple and inexpensive means to obtain rotational position data in the automotive industry is to use a Hall Effect sensor paired with a toothed wheel. Output from the sensor will be nearly sinusoidal as it senses the proximity of the ferrous teeth passing.

2.7 Transmission Error Measurement

2.7.1 Early TE measurement

National Engineering Library at East Kilbride developed the first TE measurement system for use in labs. It was later redesigned by Munro for industry. It employed 18000 pulse per revolution with encoders, from which the TTL pulses were further interpolated and compared, with the variance indicating relative angular error (TE) [4]. This method detects TE at very low speed and torque (less than 10 rpm).

Aachen Technische Hochscuhle developed a seismic method to measure the torsional vibration of meshing gears using tangentially mounted accelerometers. It is primarily used to detect once per tooth errors rather than once per revolution errors[15].

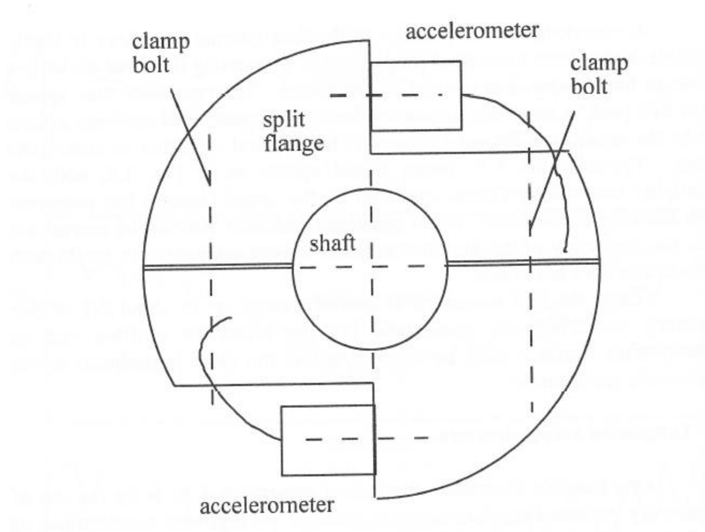

Figure 2.2 - Torsional accelerometer arrangement[4].

A third method of TE measurement was developed by Sweeney and Randall[10] which uses a high frequency timer to measure time between encoder pulses. Instantaneous shaft speeds are calculated from this, subtracted for relative speed error, then integrated to give position error (TE).

2.7.2 TE measurement using lower resolution encoders

Transmission error can be measured accurately using extremely precise encoders. Recent work has been done to develop methods for TE measurement using less precise (cheaper) encoders.

Du and Randall developed a method which involved swapping two 3,600 count per revolution encoders to assess their error[11]. They used many signal processing methods such as FFT, zoom demodulation, low-pass filtering and averaging to arrive at results which showed that the encoders were suitable to measure TE.

Remond proposed a system using a high frequency timer at 100 MHz. He accurately interpolated position between encoder pulses assuming constant velocity in these regions[12]. It was found that the limiting factor using this method is not the precision of the encoder (4,096 counts per rev in this case), but rather the rotational speed of the gear.

Smith published a paper in 2001 which showed that 5000 line encoders (using a 4X resolution mode) could be used to measure high frequency torsional vibrations[13] with frequency analysis. This corresponds to his work of investigating gear noise rather than gear faults, but has been mentioned due to the ability of rotational position sensors being used to measure these vibrations.

Endo, Randall, and Gosselin (2004) developed a technique using TE measurements to differentially diagnose between different types of gear faults[8]. Static and dynamic models were created to study variations in transmission error caused by spalling and root cracks. Root crack effects brought about changes in tooth stiffness, whereas spalling effects were determined by fault geometry.

2.7.3 Additional example of TE

Transmission Error has also been demonstrated to vary with speed. Figure 2.3 is an example of how the TE can change at different shaft speeds.

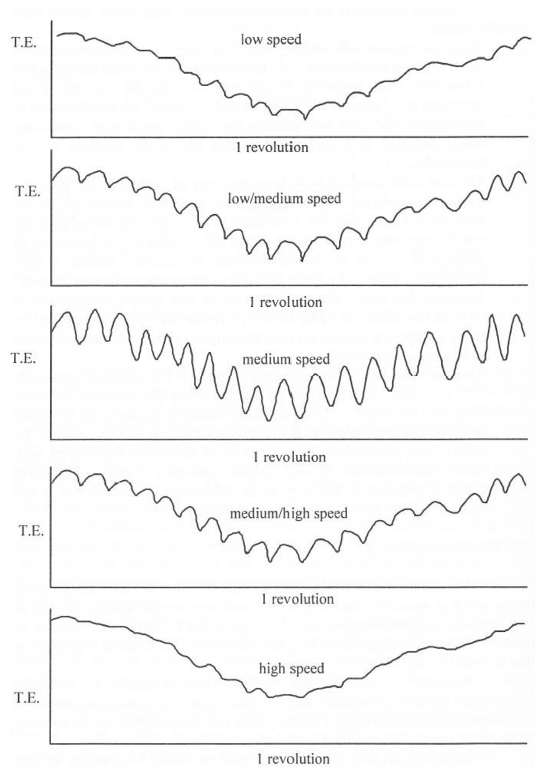

Figure 2.3 - TE variation with speed due to internal dynamics[4].

Chapter 3

Non-Contact Magnetic Rotational Position Sensor

3.1 Introduction

Chapter 2 briefly discussed the basics of several traditional encoders used in industry today. It should be made clear that these rotational position measuring devices are digital sensors with discrete resolutions. This chapter will describe the nature of the non-contact magnetic rotational position sensor used in this work. Highlights include sensor background, operation, set-up, processing to resolve position, as well as sensor error. Some description will refer to mounting on the apparatus, which is fully described in Chapter 4.

3.2 How it Works

The Hall-Effect sensor used in this application is made by Sentron AG of Switzerland, which is owned by Melexis. It is a 2-axis sensor packaged as an 8 pin small outline integrated circuit, which senses 360-degree angular position. The chip has a small ferromagnetic disk concentrator and four Hall elements placed on its edge. The disk concentrates magnetic flux, magnifying the field without amplifying noise. Only one Hall element is required for 2-axis sensing, however two are used for gain and offset benefits. The differential outputs are processed by integrated electronic circuitry which includes biasing, amplification, offset cancellation and temperature stabilization functions.

Figure 3.1 – The 2SA-10 chip, which resolves the magnetic field in perpendicular directions as a voltage.

The rotational position sensor operates by placing the unit in close proximity to a rotating magnetic field, which is supplied by a diametrically polarized magnet (See Section 3.3 - Magnet Design) affixed to the end of the shaft. The sensor is supplied with 5 VDC, and returns two voltages which are 90 degree phase shifted sinusoids relating to perpendicular magnetic field strength. This output allows 0-360 degree absolute position calculation, without any rotation to index or calibrate the sensor. In this instance, the magnetic flux was such that the sensing head was optimally 2.5 mm from the magnet to ‘nearly saturate’ the sinusoid signal. Greater distances decrease the amplitude of the sinusoid, reducing resolution.

3.3 Magnet Design

Two puck shaped magnets were provided from our industry sponsor, which were polarized diametrically as shown in Figure 3.2 below.

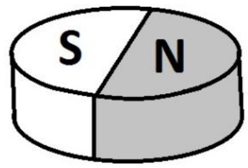

Figure 3.2 – Diametrically polarized magnet.

Figure 3.3 is a diagram of magnetic field lines on a simple bar magnet, and how they can be simplified as a single vector. As mentioned previously, the sensing chip projects the magnitude of this vector into perpendicular directions, which is akin to taking the x and y magnitudes of a vector.

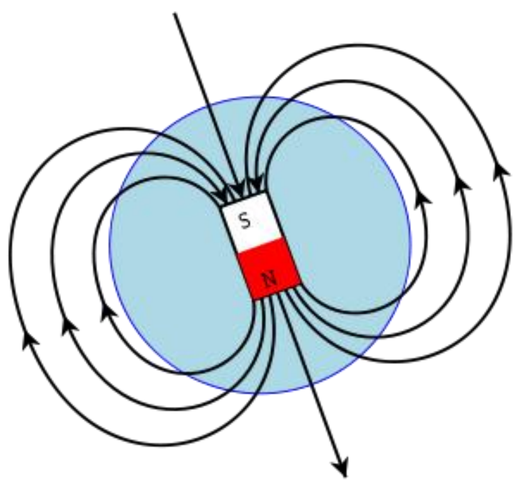

Figure 3.3 – Example of the magnetic field around the magnets.[14]

3.4 Magnetic Considerations

A magnet must be fixed to the shaft capable of providing a magnetic field in the range of up to 1000 mT at the position of the sensing head. For many applications there will be size constraints on the magnet, necessitating the use of rare earth magnets. One must also consider the harsh environment of a gearbox, where shock and vibration as well as a potentially hot environment must be tolerated. Samarium Cobalt was selected as it exhibits a strong resistance to demagnetising during thermal cycles and contact with other magnets prior to mounting on the shaft.

3.5 Setup

The magnets were mounted in custom recessed aluminum extensions which fit together with the shaft. These extensions made it possible to solidly glue the magnets to a removable piece, allowing shafts to be changed without the need to remove and reattach the magnets. It also moved the magnets closer to the exterior of the gearbox for optimal sensing head placement.

The sensing heads were held in place by a bracket which permitted axial adjustment in order to optimize sensor resolution. This was done using an oscilloscope while the gearbox was in operation, moving the sensing head close to the magnet without saturating the signal. The optimal distance for this particular arrangement was found to be 2.5 mm.

3.6 Signal Processing to Obtain Rotational Position

There are several steps required to resolve shaft position from the raw sensor output (see Figure 3.4).

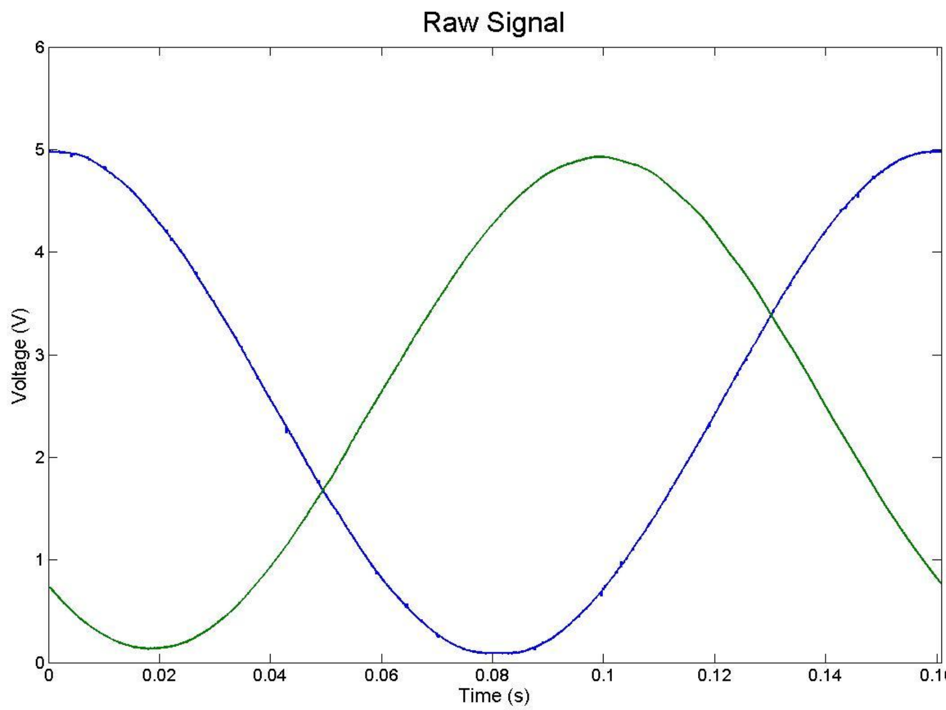

Figure 3.4 – Example of the raw sensor signal for one shaft (single rotation).

First, the 0-5 V sinusoid must be normalized to fit in the range of -1 to 1. This was done by finding the maximum and minimum values for each sinusoid and then shifting and scaling appropriately (as seen in Figure 3.5).

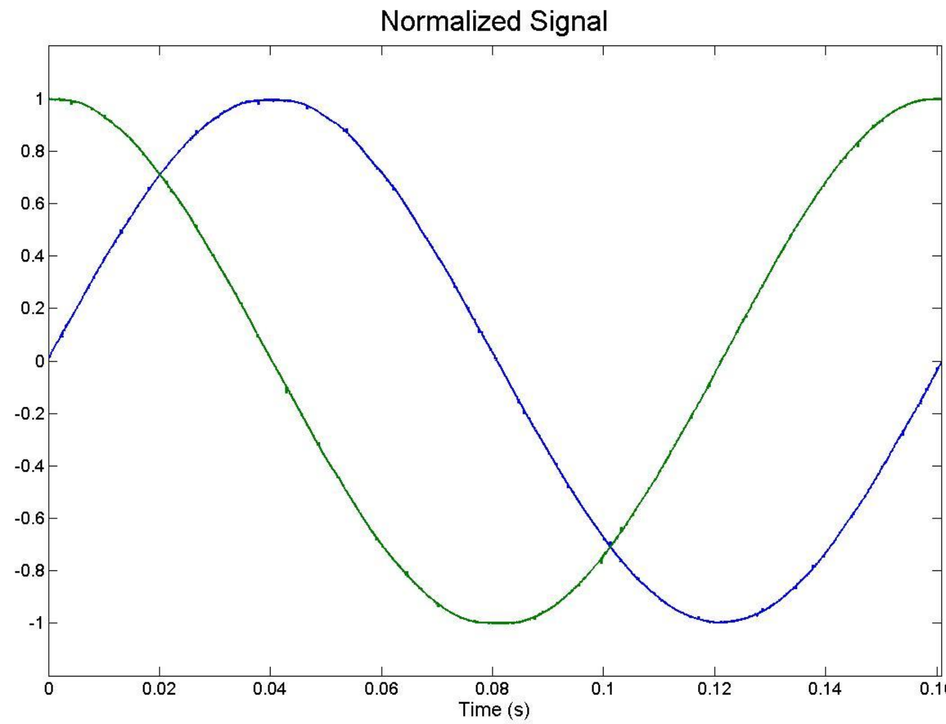

Figure 3.5 – Example of a normalized signal for a single shaft.

These signals were then conditioned by a 2 input arctan function in Matlab. The function (atan2) takes both sine and cosine inputs and returns a position from -180 to 180 degrees (See Equation 3.1, Figure 3.6).

$$position(°) = atan2(input1, input2)\frac{360}{2\pi} \qquad (3.1)$$

It is important to recognize that the 360 degree position is known because the sine and cosine inputs are examined separately. Location can be resolved from a single sine or cosine input, though it only details the position of a half rotation and is ambiguous unless the position is incremented by 180 degrees. The resolution of single sinusoid position is best when close to zero, however it suffers around the peaks when small changes in amplitude correspond to large changes in position. By utilizing the two sinusoids, the net effect is a compromise of changing resolutions which are out of phase, improving position resolution greatly. Furthermore, two sinusoids which describe the same position are somewhat redundant, which reduces the effect of a disturbance to a single sensor output. The resolved position for a single shaft is illustrated in Figure 3.6.

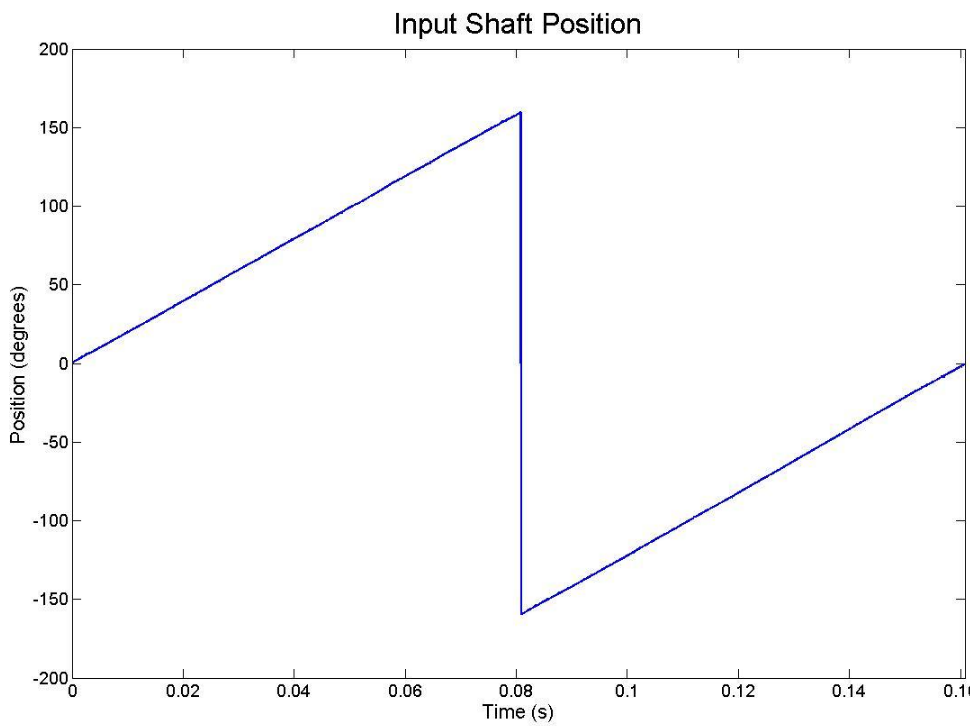

Figure 3.6 – Example of resolved shaft position for a single shaft.

3.7 Sensor Error

A review of the non-contact magnetic sensor would not be complete without a measure of its performance as measured by a traditional optical encoder. This was carried out by properly setting up the sensor as described above in Sections 3.5 and 3.6, as well as installing a BEI 360 pulse incremental encoder on the same shaft. The resolution of the encoder is obviously +/- 0.5 degrees, however the pulses are extremely accurate. Resolved sensor positions at these extremely accurate single degree increments were recorded, with the variations over a complete rotation depicted in Figure 3.7. Un-calibrated sensor error was found to being in the range of +/- 0.5 degrees.

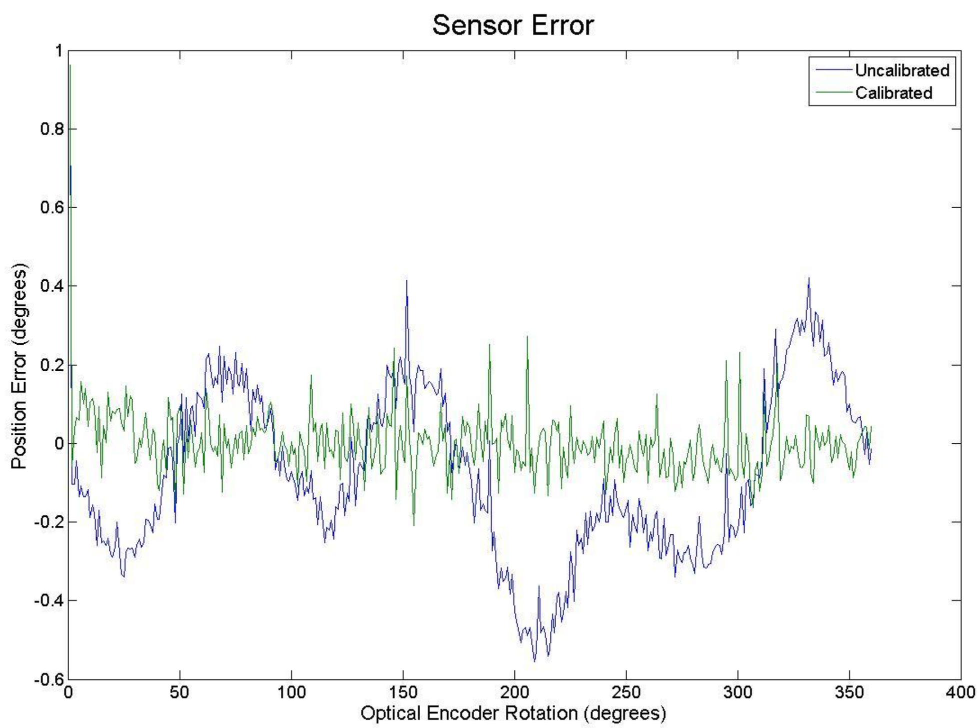

Figure 3.7 – Sample of sensor error, as measured by a 360 pulse incremental encoder.

It is sinusoidal at 4X shaft rotation speed which is due to small misalignments in sensing head orientation. Examination of further rotations shows that the error remains regular within approximately +/- 0.15 degree. The error also has a dynamic aspect to it, where increasing shaft speeds will increase (in very small magnitudes) a separate but related sinusoidal error. This has been postulated to be caused by magnetic induction in the sensing circuitry. Confirmation of the cause of this dynamic variability was not possible within the scope of this work.

3.8 Sensor Orientation

In testing, the sensing head has been placed along the axis of rotation in close proximity to the end of shaft as the manufacturer originally intended. Included in this thesis as an appendix (Appendix A - Magnetic Sensor Response at Different Orientations) is an investigation of alternative sensor orientations which could be pursued should size and space constraints make the end of shaft arrangement impossible. Figure 3.8 shows the standard non-contact magnetic sensor arrangement of puck style magnet (light gray) and sensing head (darker gray). Figure 3.9 shows an alternate configuration that, while exhibiting some loss in resolution, could be used in space constricted locations.

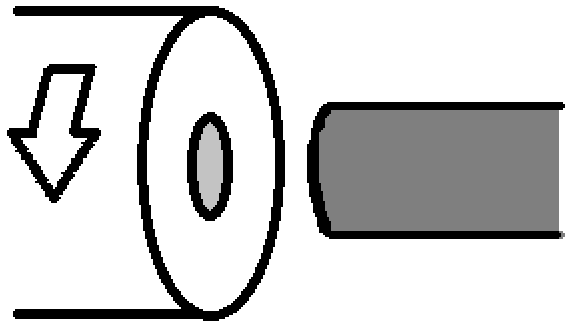

Figure 3.8 – Conventional magnet/sensor arrangement.

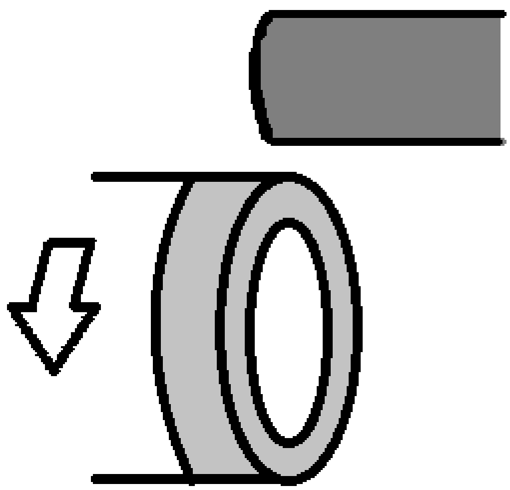

Figure 3.9 – Ring magnet with axially facing sensing head.

3.9 Conclusion

This chapter introduced and detailed sensor setup, operation, and error. It will be shown in Chapter 5 that for the purposes of this thesis, sensor error is not significant as basic filtering can eliminate these low frequency errors, allowing for the detection of gear faults.

Chapter 4

Method and Apparatus

4.1 Introduction

With the non-contact magnetic rotational position sensor having been described, the application selected to evaluate sensor performance will now be introduced. This chapter describes the gearbox, data acquisition system, gear selection, as well as the individual faults initiated in the gears for detection.

4.2 Gearbox

A gearbox dynamics simulator (manufactured by SpectraQuest Inc.) suitable for testing AC motors, gears, and bearings using vibration or other data was available for use in the Dynamics Research Group at Queen's University. The gearbox is a parallel shaft single gearbox incorporating an AC motor, an electronic brake load, and sufficient mounting for instrumentation (some of which are indicated in

Figure 4.1). The schematic in

Figure 4.1 does not show the accelerometer, microphone, or the two optical encoder placements. The encoders were situated opposite the magnetic sensor on each shaft (Figure 4.2 shows accelerometer, input optical encoder and output magnetic sensor).

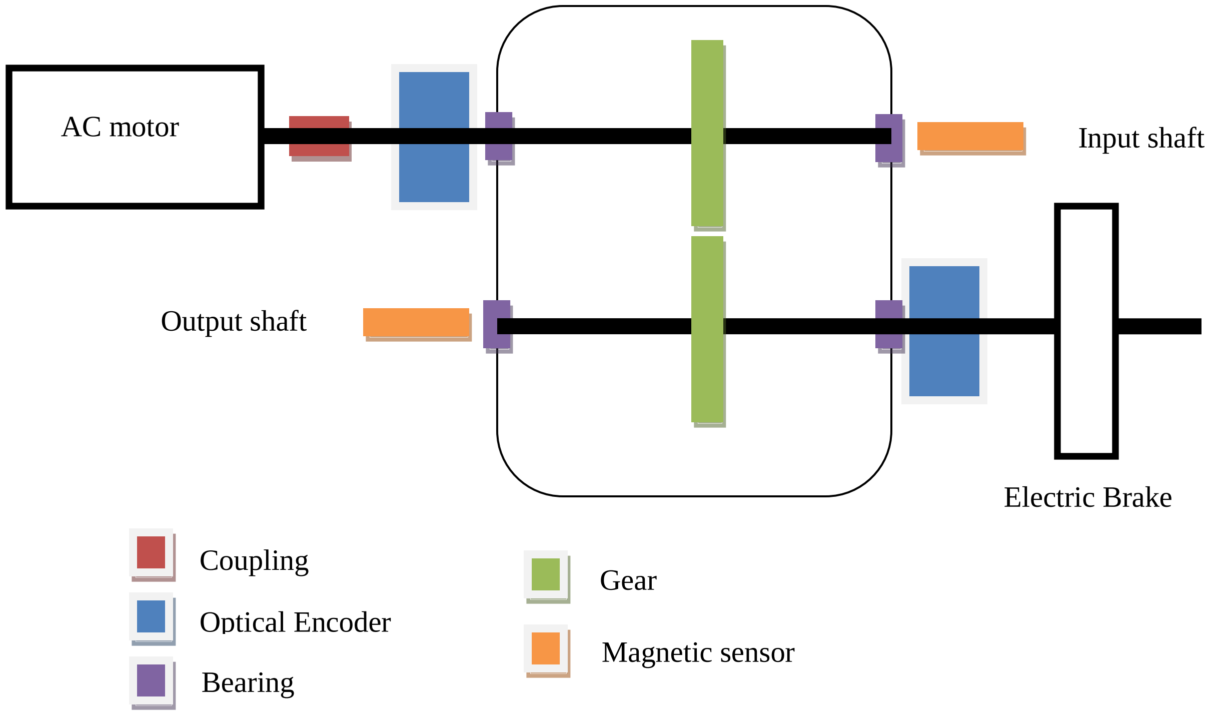

Figure 4.1 – Schematic diagram of gearbox and magnetic sensors.

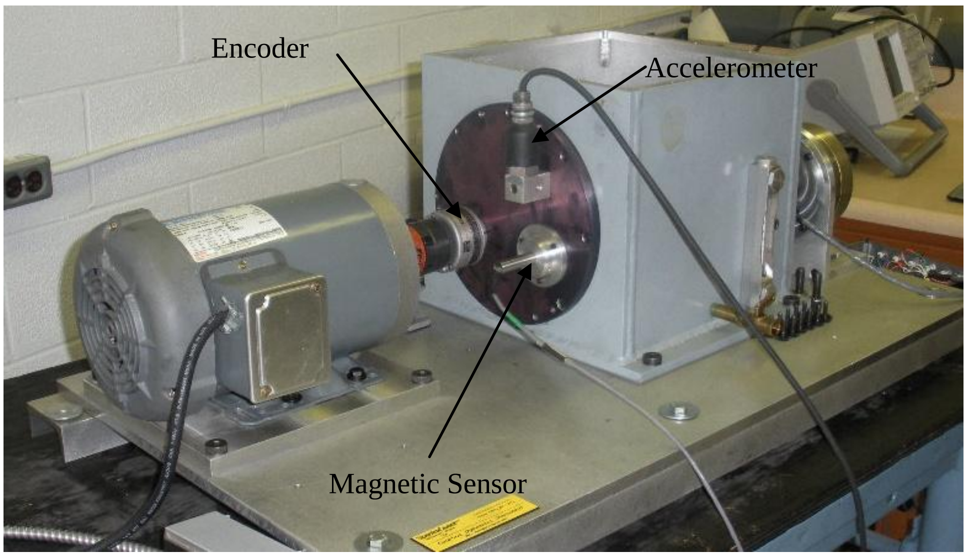

Figure 4.2 – Gearbox rig with input shaft optical encoder, accelerometer, and output shaft magnetic sensor visible.

The incremental optical encoders used in this application were 360 pulse BEI Express Encoders (Model number XHS25F-37-R1-SS-360-ABZC). They have two channels (A and B) that output position 90° out of phase, as well as an indexing channel (Z) to mark once per revolution. The inverse of these three signals are also output, which is denoted by the 'C', or complementary output. Due to constraints with data collection, only one channel per shaft (A) was recorded. A further description can be found in Section 4.3 - Data Acquisition). A closer look at shaft position sensor mountings is found below in Figure 4.3.

The accelerometer used in testing was rigidly mounted to sense vertical vibrations directly above the output shaft. Its mounting position is shown in Figure 4.2. A microphone was also used during testing, and was positioned on the base of the test-bed underneath the electronic brake load (approximately shown in Figure 4.5).

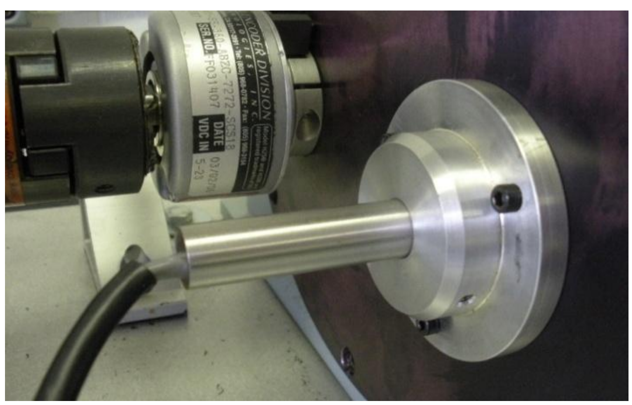

Figure 4.3 – Close-up of output shaft magnetic sensor and input shaft optical encoder.

The motive source to the gearbox rig was a 3 hp Marathon single phase AC electric motor (visible in Figure 4.2). It was controlled by a Delta VFD-A motor controller, which made repeatable speed control possible. The motor was connected to the input shaft via a LoveJoy coupling (Figure 4.4).

Figure 4.4 - LoveJoy coupling used to transmit power to the input shaft.

The gearbox was loaded by an electric brake from Warner Electric (Figure 4.5). It is manually controlled by a voltage between 0 and 12 volts.

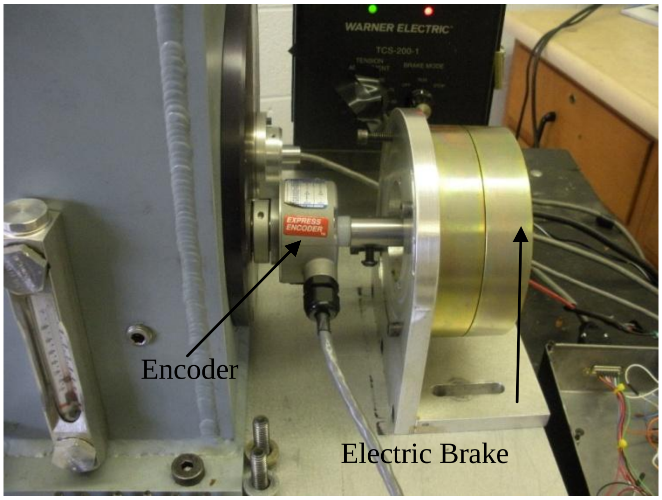

Figure 4.5 – Output optical shaft encoder and Warner Electric brake used to load the gearbox.

4.3 Data Acquisition

Data was simultaneously sampled using a National Instruments PXI data acquisition system running Labview 7.1. Three separate cards were used in order to correctly sample at three different frequencies for different instruments. Shaft position was sampled at 50 kHz on a PXI-4472B card. This high frequency was required because of the shaft speed and the frequency of the TTL pulse generated by the optical encoders used. Two channels were required for each non-contact magnetic shaft encoder, as well as a single channel monitoring each express encoder (6 channels total for position). Due to data file size constraints as well as the card being limited to 8 channels total, it was decided that 4X interpolation on the encoders (requires two channels per encoder) would be excessive, therefore only a single channel per shaft was used.

Sound and vibration were sampled by a microphone and accelerometer at 10 kHz on a PXI-4472 board. This sampling rate has proven adequate in the past and was included in data collection for fellow researchers to assess gear health using traditional noise and vibration analysis.

Each file recorded 5 seconds of data in order to capture a large number of shaft rotations. For each combination of gear condition and load, at least 150 files were documented.

4.4 Variable Load

Different brake loads were used to observe differences in the transmission error and gearbox dynamics. Using a controllable DC power supply, brake loads of 3.5V, 5V, and 6V were selected at the beginning of the testing. The motor was found to almost stall when a loading of 7.5V was applied, so these three load levels were chosen based on observation. These loadings will be referred to as partial, full, and overload. The corresponding torque was not measured for each voltage.

4.5 Gears

Early testing on steel gears (Martin Sprocket & Gear Inc, Part Catalogue Numbers TS1648, TS1680) had been inconclusive despite applying numerous techniques. It is believed that despite the amount of damage inflicted to the gears, due to the tooth mesh ratio and general robustness of the gears, the motor/load combination could not cause significant tooth deflection to allow detection. Additionally, sensor performance was unknown, so the goal of detecting transmission error and gear health was re-evaluated.

4.5.1 Material Selection for New Gears

It was decided that a new set of gears would be obtained, which would be weaker and more flexible. After speaking with representatives at numerous gear suppliers, it became clear that our desired traits for the gears were contrary to anything on the market. There were some alternative materials such as Delrin or softer metals, however they did not seem suitable.

The next logical step was to manufacture gears in house, relaxing the constraints of gear size, shape and material. Plastic seemed to be the preferred material, however the design and manufacturing method remained to be determined.

4.5.2 Gear Profile Design

Parametric CAD software (Solid Edge v17) was used to generate a spur gear profile (Figure 4.6). The face width was 0.5 inch (12.7 mm), and the pitch diameter was sized such that a 1:1 gear ratio would be possible. This was deemed to be important as benefits in later post-processing could be realized. The early testing of steel gears had a 5:3 reduction, necessitating the examination of transmission error with respect to the ‘gear period’ or amount of rotation the gears must undergo until the same teeth interact again. When using a 1:1 gear ratio all tooth meshes remained constant. That is, the same teeth on both gears meshed together every shaft rotation.

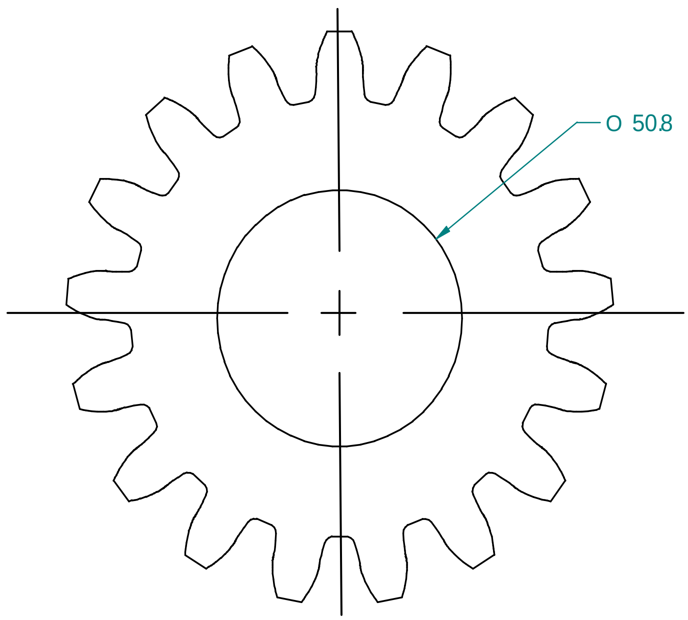

Figure 4.6 – Spur gear profile generated in Solid Edge.

One of the beliefs from early testing was that transmission error would be easier to detect using larger but fewer teeth. Due to diameter constraints and the preference of fewer teeth, a design with 17 teeth was generated.

4.5.3 Rapid Prototyping

The next obstacle was manufacturing technique. It was proposed that the gears could be cut using a waterjet CNC cutting machine, however this led to consideration of alternative manufacturing techniques. Queen’s University is equipped with a Dimension SST 1200es 3D printer.

This printer makes 3 dimensional objects by ‘printing’ melted ABS plastic in the profile specified by a .STL file generated from CAD software. After the profile has been printed, the head increments by 0.010” or 0.013” (layer thickness) and continues building the part. This particular model of 3D printer can generate a wide variety of shapes and even complicated moving parts by printing dissolvable ‘filler’ material (soluble support). The soluble material is sodium hydroxide, and is dissolved in a water based solution.

Upon consideration of the material (ABS plastic), concerns with sliding friction reaction to oil were addressed. It was concluded that the plastic would wear over its brief lifetime in gearbox testing while running un-lubricated, making gear degradation over time a potential pursuit. Therefore, mounting hardware to affix the plastic gears to the shaft was designed, and the plastic gears were ‘printed’ by the rapid prototyping machine (Figure 4.7).

Figure 4.7 – Completed plastic spur gears.

4.5.4 Mounting Hardware

The plastic gears were held on the shafts using steel mounting hardware as shown in Figure 4.8. They were designed to fit on the shaft and keyway in the same manner a conventional gear would be held. Four bolts are used to squeeze the plastic gear profile and rigidly secure it to the shaft. There is a small ridge in the collar side of the mounting hardware which the plastic gear fits on to, as this is what centres the gear. Great pains were undertaken to find the true center of the gear by the technicians in the machine shop, with the goal of smooth running of the gears without eccentricities.

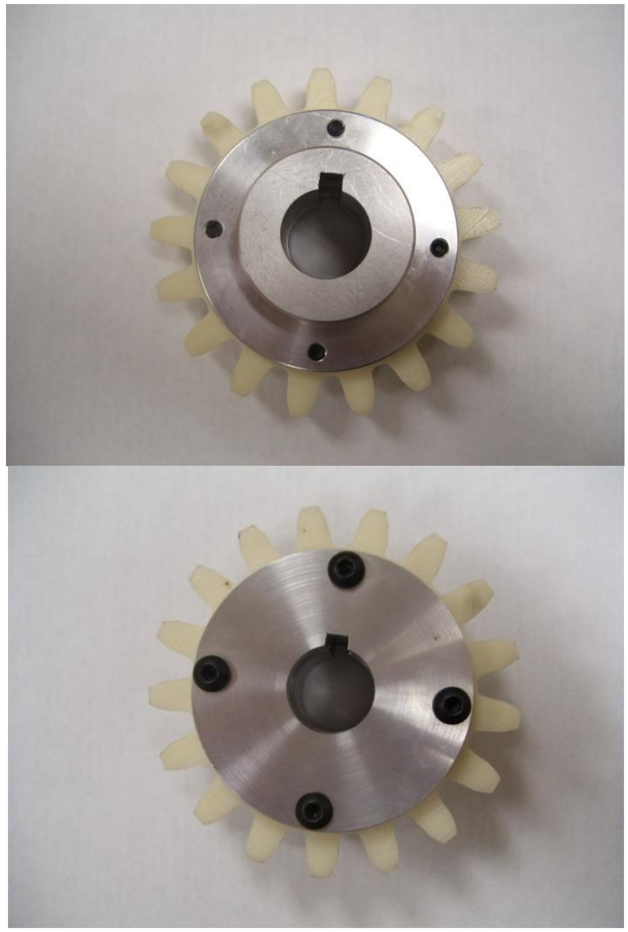

Figure 4.8 – Mounting hardware, including plastic gear.

Due to the resolution of the printing head, there was some surface texture on the gear faces. To reduce the change in gear surface roughness while testing artificially induced faults, the gears were broken in by running for several hours. Data was sampled periodically with the intent of discerning changes in gear box dynamics over the first few hours of operation without external influence. Once the set of gears had been run in, benchmarks were recorded for each respective load level.

4.6 Artificially Induced Faults

4.6.1 Flat Tooth

The first fault induced in the testing was intended to replicate damage to one face of a single tooth. It is an extreme example of localized material removal, which in this case was removed with a rotary grinding tool (see Figure 4.9). The purpose of this induced fault was to interfere with the involute curve and create a once per revolution fault in the relative shaft position measurable by the rotational position sensors. This damage was located on the driving side of an input tooth (right side of the middle tooth in Figure 4.9).

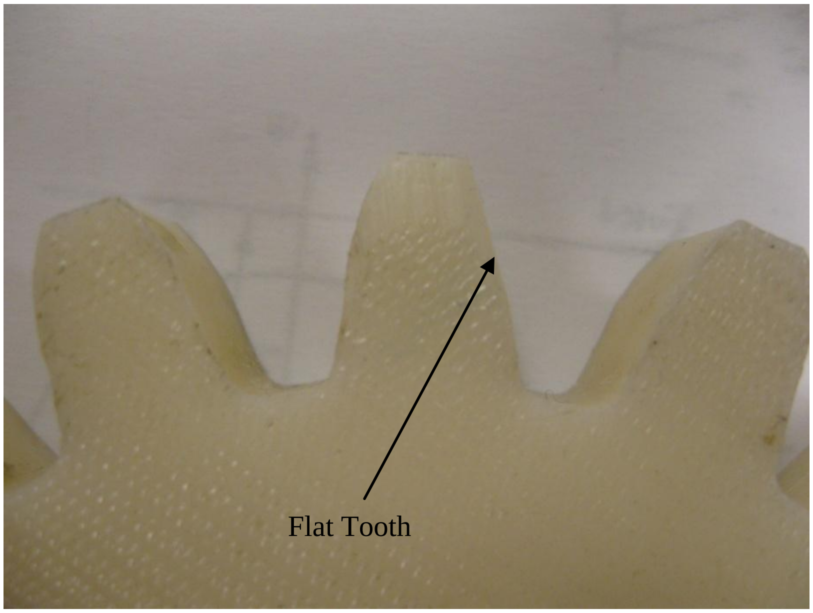

Figure 4.9 – Damage inflicted on input tooth.

4.6.2 Two Flat Teeth

The next fault was a continuation of the flat tooth described previously. It was induced with the intention of further damaging the smooth involute relationship of the gears. Without moving any sensing equipment or hardware, a similar ‘flat tooth’ was created through material removal to the mating tooth on the output gear (as seen in Figure 4.10, photo taken after removal from the gearbox).

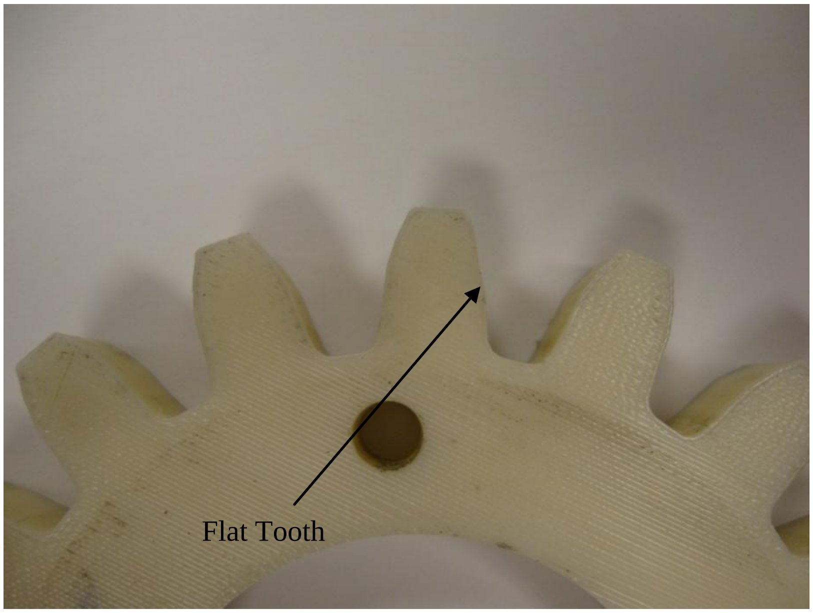

Figure 4.10 – Flat tooth on output gear.

Viewed individually, these faults are not obvious, so Figure 4.11-Figure 4.14 were generated to show the interaction of the flat teeth.

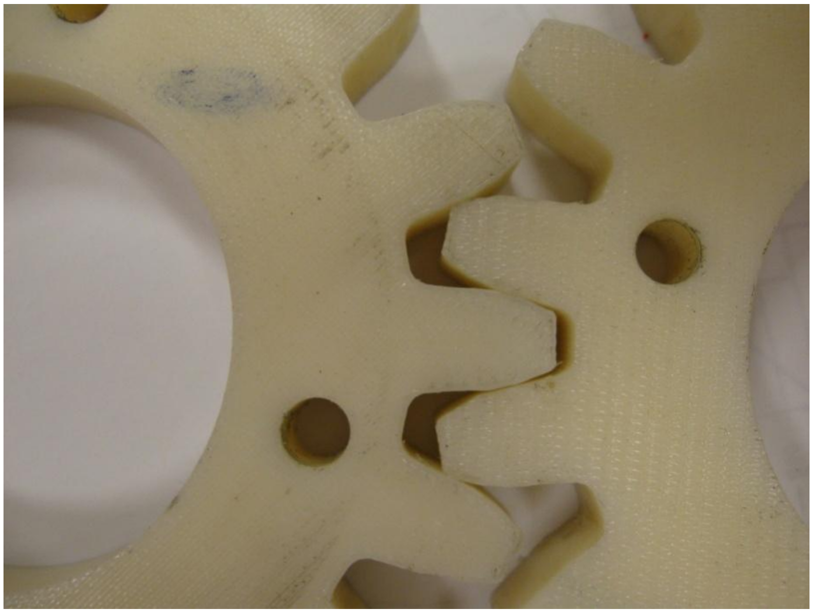

Figure 4.11 – Normal teeth in engagement.

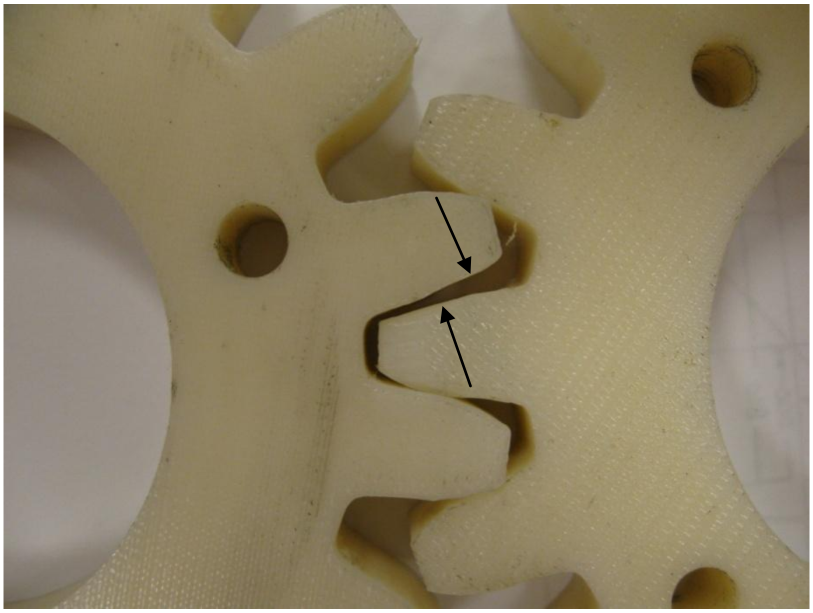

Figure 4.12 – Two flat teeth entering mesh.

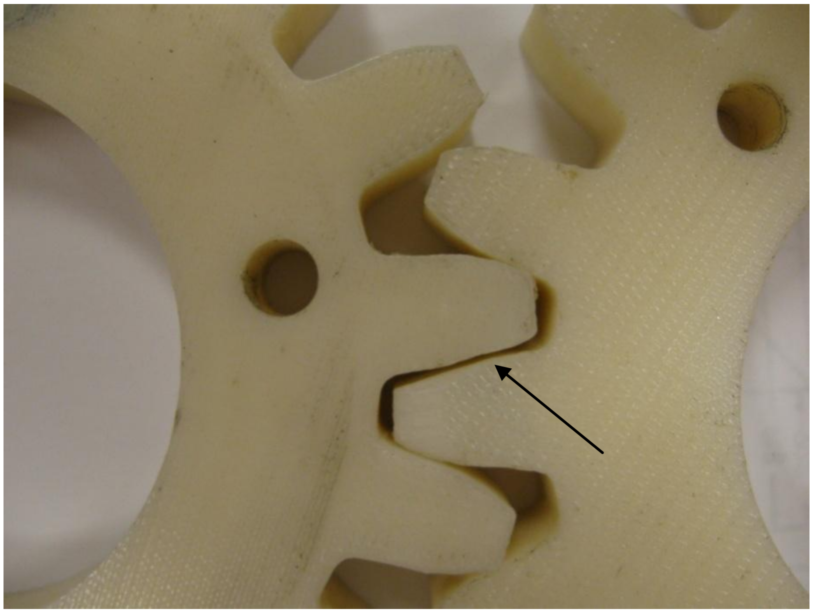

Figure 4.13 – Two flat teeth meshing together.

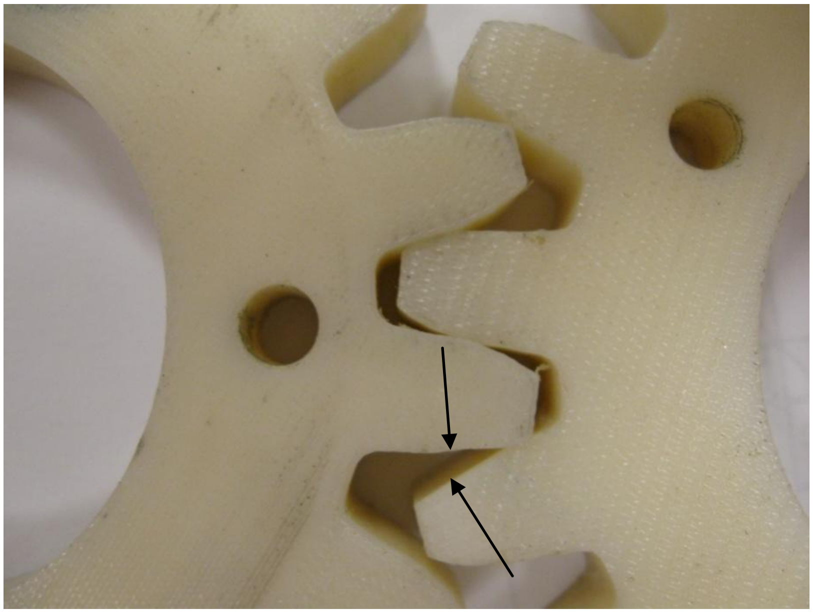

Figure 4.14 – Two flat teeth near the end of mesh.

Figure 4.11-Figure 4.14 should give a clearer understanding of how the gearmesh was affected by these faults. It should be noted in Figure 4.12 that the adjacent teeth are in contact, creating a definite gap between the 'flat meshing pair'. Figure 4.13 and Figure 4.14 show how the mesh progresses and ends with a poor handoff to the next pair.

These figures were generated by placing the gears together on a flat surface without restrictions to their center to center distance. It is with this in mind that they not be taken as the gears literal interaction, rather an example which better showed the material removal and change in the involute curves.

4.6.3 Second Set of Gears

A new set of gears was generated by the rapid prototyper, and mounted to the shaft collars by the staff of the McLaughlin Hall Machine Shop, taking great care to locate the center properly and minimize eccentricities. This gear set was also broken in for several hours and benchmarked over the load range. This was included because it was suspected that at this level of refinement, any gear combination will create a different signature, therefore it is important to observe relative changes in operation rather than differences unique to manufacturing variances.

4.6.4 Progressive Root Crack

The second type of artificial induced fault was a root crack. This was selected with the intent that individual tooth flexion could be detected. Once again, modification of the tooth was performed without removing any sensing or mechanical equipment from the test rig. A rotary cutting tool cut into the root of the tooth on each side (as seen in Figure 4.15).

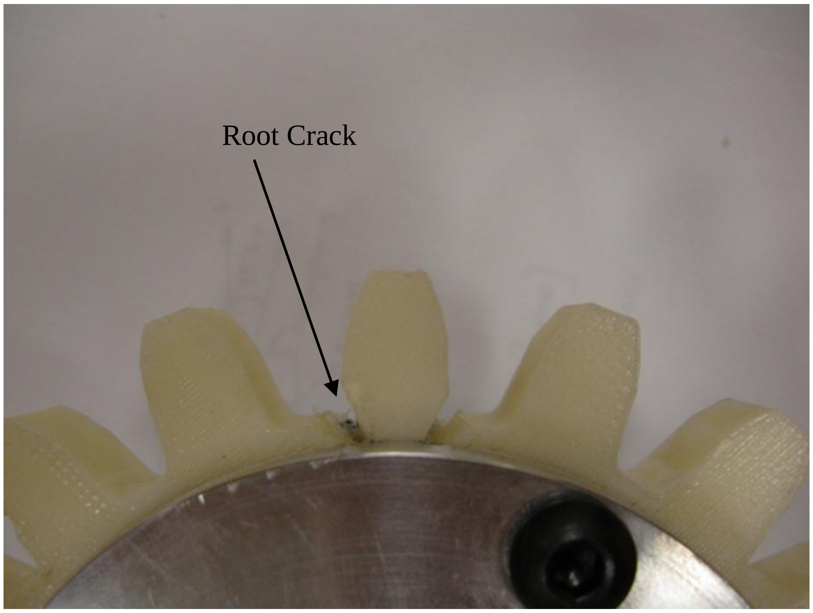

Figure 4.15 – Root crack – photo taken after tooth had failed.

The first cut was approximately 1.5mm deep across the entire face width of the tooth. Upon a full cycle of testing at different loads, the depth was increased to 3mm each side. These were measured by estimating the depth of the cutting head after each modification. Midway through testing at the medium load level, the tooth was flexing freely, and fell out when prodded gently.

4.7 Conclusion

This chapter has introduced the gearbox dynamics simulator and the array of instruments monitoring it. Data acquisition and sampling rate were also discussed. It has also explained the logical choice to manufacture plastic gears in house due to material selection, desired profile, and ease of acquisition. The method of wearing in the gears and the subsequent testing regime for the two induced gear faults was also detailed. Chapter 5 details results obtained using these methods.

Chapter 5

Results

5.1 Introduction

This chapter chronicles the range of results achieved using the non-contact magnetic rotational position sensor on a gearbox dynamics simulator. It covers the development of analytical techniques used in this pursuit of gear fault identification, from early work with the steel gears, to definitive results with plastic gears.

5.2 Preliminary Results

At the project's inception, sensor behaviour and mode of operation were unknown. Initial testing with the magnetic sensor to determine its abilities was conducted by recording and analyzing data from the sin output only. As detailed in Section Chapter 10, the ability of the sensor to resolve 360 degree position is dependent on an arctan function using sine and cosine inputs. With solely sine data, quadrant position could only be inferred, and rotational position was found by increasing the position of the shaft in increments of 180 degrees. Despite this, shaft position could be resolved, though resolution suffered relative to proper position calculation.

At this stage in analysis development, the shaft position over a complete revolution was subtracted from the ideal shaft position of a perfectly steady rotating shaft. This is based on the definition of Transmission Error (TE) by Smith[15]:

> ***"...TE, and is defined as the difference between the position that the output shaft of a gear drive would be if the gearbox were perfect, without errors or deflections, and the actual position of the output shaft. It may be expressed either as an angular displacement from the 'correct' position or sometimes more conveniently as a linear displacement along a line of action, i.e., at the base circle radius or as a linear displacement at pitch circle radius."***

The importance of this quote is twofold. First, the definition of transmission error as the difference in measured and ideal output shaft positions assuming a perfectly rotating input shaft, and second, introducing linear displacement at pitch circle radius as a measurement of TE. All following work pertaining to transmission error has been completed using linear displacement at pitch radius. Additionally, since the input shaft is not rotating at a perfectly steady speed, transmission error is calculated as the relative shaft position (found by subtracting input and output shaft linear displacements at pitch radii).

Returning to the case of shaft position being subtracted from its ideal position, early results were poor. Around this time, it was recognized that combining sine and cosine outputs could resolve 360 degree position, and the method of subtracting the more accurate shaft positions would be pursued.

In the case of the steel gears used at the beginning of the project, the apparatus as described in Chapter 4 is not accurate, as an output shaft optical encoder had not yet been obtained, and the sampling rate for all channels was 10 kHz. This, as well as the gear reduction, led to problems while attempting to increase the signal to noise ratio. In order to increase the amplitude of repetitive faults and decrease random signal noise, raw sensor data was synchronously averaged by adding up sinusoids from consecutive shaft rotations and then subtracting a perfect sinusoid of the same magnitude. By doing this, faults occurring at the same position on a gear would remain the same, and non-synchronous parts of the signal would cancel out and minimize. Since the tooth ratio was 48:80, using an input shaft rotation or an output shaft rotation as the period would cause regular events from the other shaft to disappear. In order to simultaneously observe faults occurring on both shafts, a common period of 5 input shaft rotations and 3 output shaft rotations was used. This is also the period where, if a tooth was marked on the input gear, it would match up with the same output tooth after 5 input shaft revolutions. It can be found for any gear pairing by the lowest common denominator of tooth counts (48 and 80 have 240 in common). Figure 5.1 shows the locations on the output gear where the input tooth would mesh during 5 input shaft rotations.

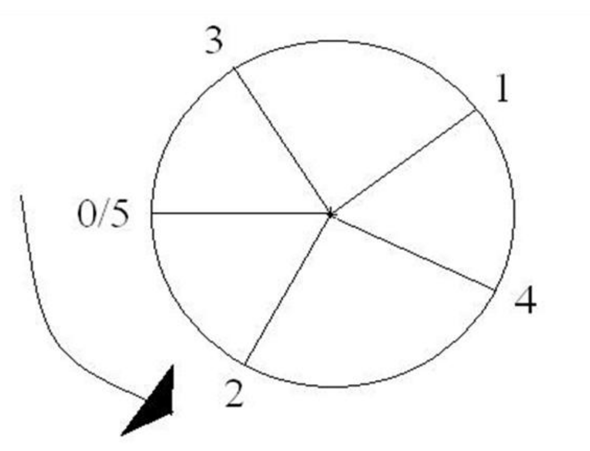

Figure 5.1 – Locations on output gear where a marked input gear would mesh.

Using this gear period, the amplitude of synchronous events could be maximized with respect to signal noise. Transmission error was then calculated by subtracting input and output shaft positions. A breakdown of processing steps is outlined in Figure 5.2.

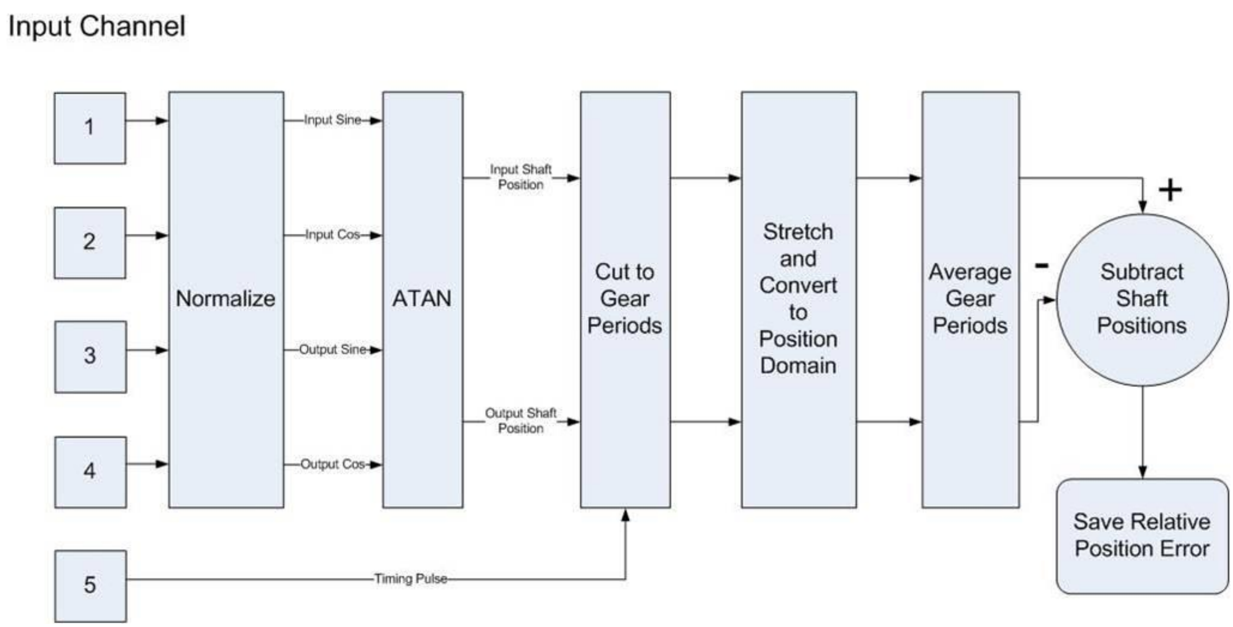

Figure 5.2 – Processing steps to obtain relative position error.

This sequence of data processing resulted in Figure 5.3**Error! Reference source not found.**, which spans the duration of a five input shaft rotations (or one 'gear period'). As will be discussed later, the low frequency (and large magnitude) periodic signal is the interaction of sensor error at two different frequencies.

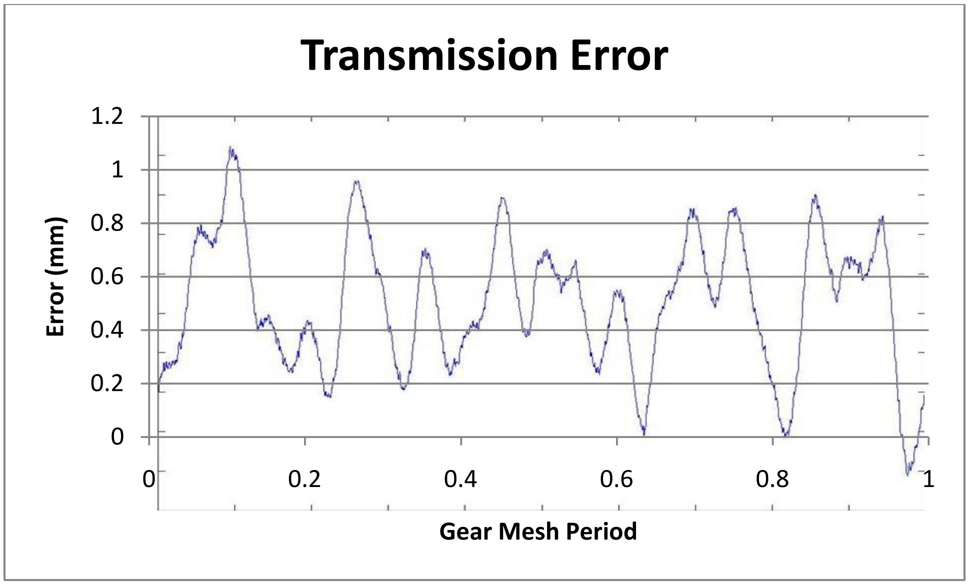

Figure 5.3 - Transmission error of steel gears over a complete 'gear period'.

Upon closer inspection of Figure 5.3, it is clear that some gear tooth dynamics are being sensed by the magnetic position sensor. This is revealed in Figure 5.4. The larger magnitude peaks that deviate from the slower oscillating signal correspond with the vertically hatched lines on the figure. These lines are set at the expected gear tooth frequency.

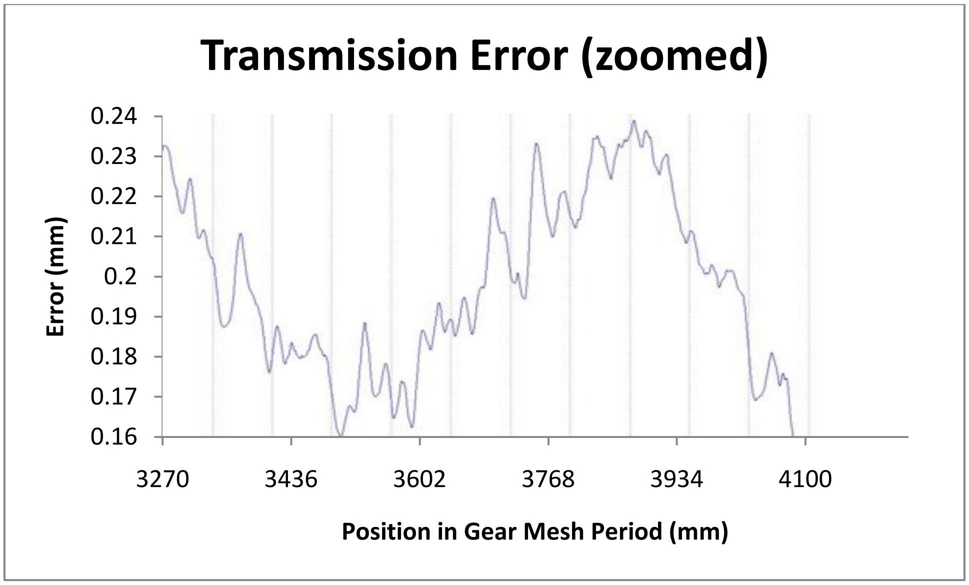

Figure 5.4 - Zoomed in sample of Figure 5.3. Note the regular spacing of peaks with respect to vertical hatched lines.

This observable trait is further detected by a Fast Fourier Transform (FFT) of the gear period data (see Figure 5.5), which shows frequency peaks at shaft orders and the gear mesh frequency.

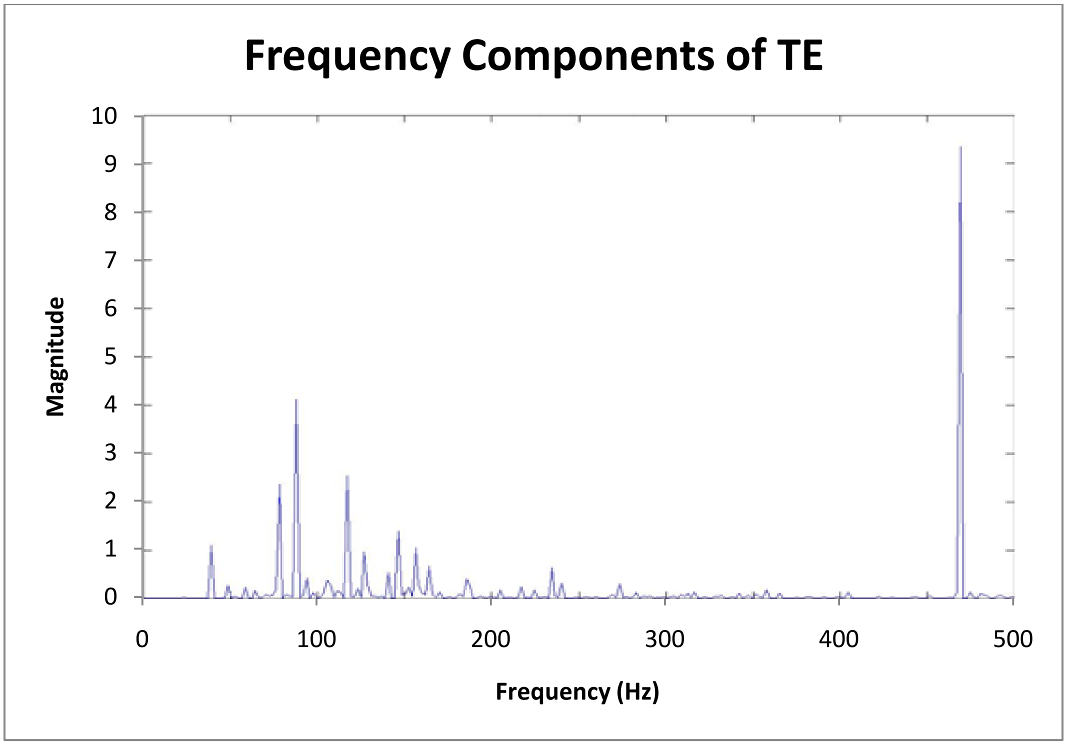

Figure 5.5 - FFT of Figure 5.3. Large peak corresponds to 2X gear mesh frequency.

At this point in the research, a fresh start was deemed necessary. Gear mesh appeared to be detectable, but not differentiable between the good and fault induced steel gears on hand.

5.3 Plastic Gear Data Processing

With a new set of gears came a 'back to basics' approach on data processing. Shaft positions were resolved for both the magnetic sensors (as described in Section 3.6) and the optical encoders. The relative shaft displacements were then found by subtracting input and output shaft positions. An example of this can be found below in Figure 5.6. As noted in Section 3.7, there is a '4X shaft speed' position error for the magnetic sensor. This is further compounded by subtracting two shaft positions. The sensors have similar but different/offset error, so the result seen in Figure 5.6 is a combination of these interacting errors.

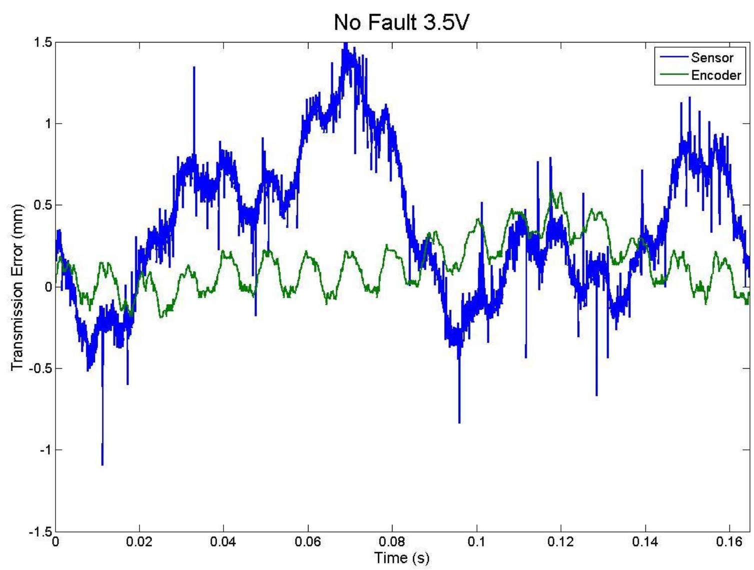

Figure 5.6 - Simple subtraction of shaft displacements at pitch line for one rotation.

In order to eliminate this repetitive error, a 'zero-phase window average' filter was employed to reduce the lower frequency variation in sensor signal. Using a window width of 200 data points (found through trial and error), it was effective at removing the low speed error, resulting in a noisy signal perfectly centered about zero as seen in Figure 5.7. This window spans a time period of 0.004 seconds, or approximately 40% of a tooth in rotation.

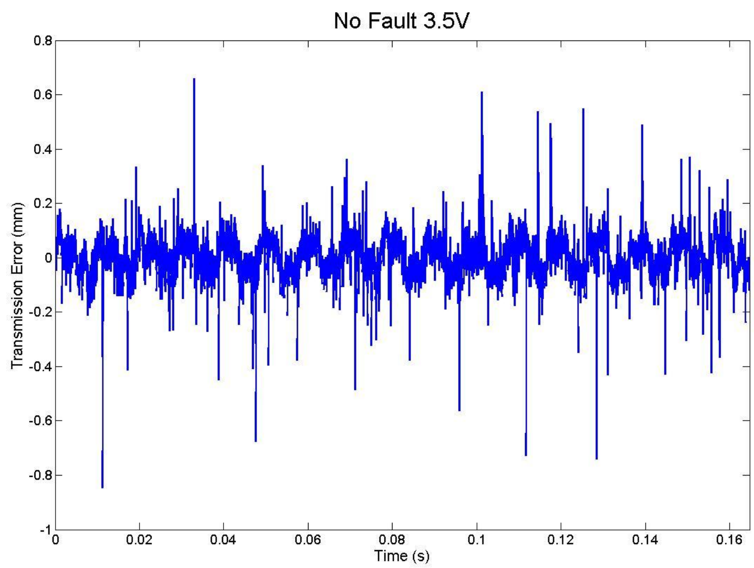

Figure 5.7 - TE from sensor after removing low frequency error.

This was deemed to be 'too noisy' for effective characteristic feature extraction (more on this later in Section 5.5), so an additional window filter (optimally found to be 120) was used to remove the high frequency noise. This window is 25% of a tooth`s rotation. The calculation for transmission error used to generate the results in Section 5.4 is shown in Equation 5.1.

$$TE(final) = moving\ average[TE(raw), 120] - moving\ average[TE(raw), 200] \quad (5.1)$$

5.4 Plastic Gear Transmission Error Results

Due to the large amount of test cases, results for the 5V full load condition will be presented in this section as they are a good representation of the three loadings. Each figure depicts one full revolution of the input and output shafts. Full results can be found in Appendix B.

The second set of plastic gears used for root crack testing bear a '2 –' in the titles and filenames to differentiate from the first set. Two sets of results are included for the 5V full load condition of '2 Deep Root Crack' from early and late during data collection as the induced fault progressed to full tooth failure during this testing.

Due to data corruption, the No Fault 6V overload condition is unavailable for the first set of plastic gears.

5.4.1 Flat Tooth Fault

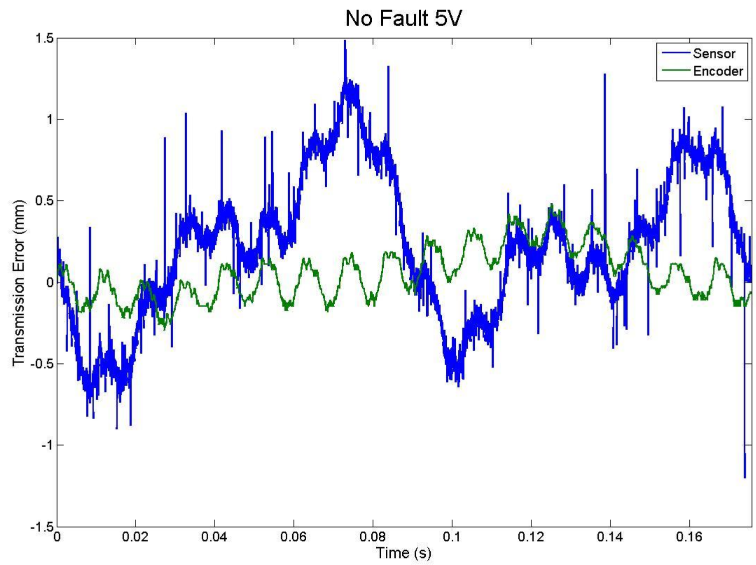

Figure 5.8 – Raw TE for No Fault condition at full load.

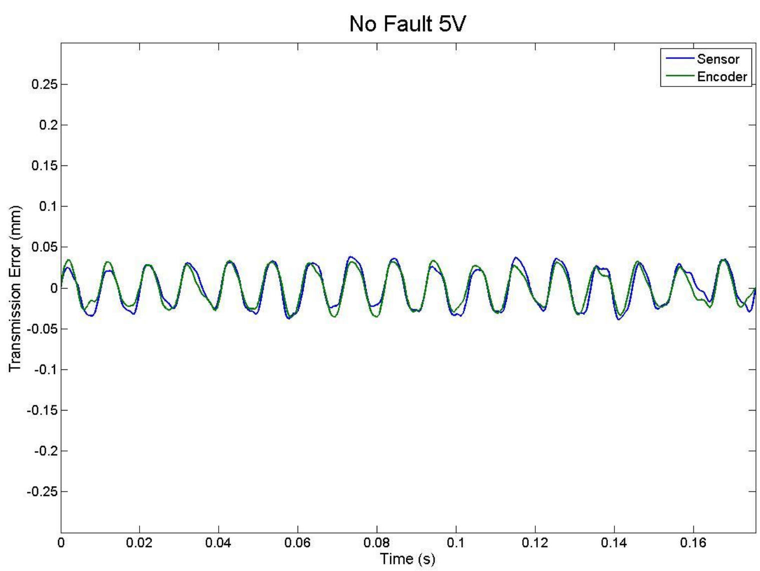

Figure 5.9 - Filtered TE for No Fault condition at full load.

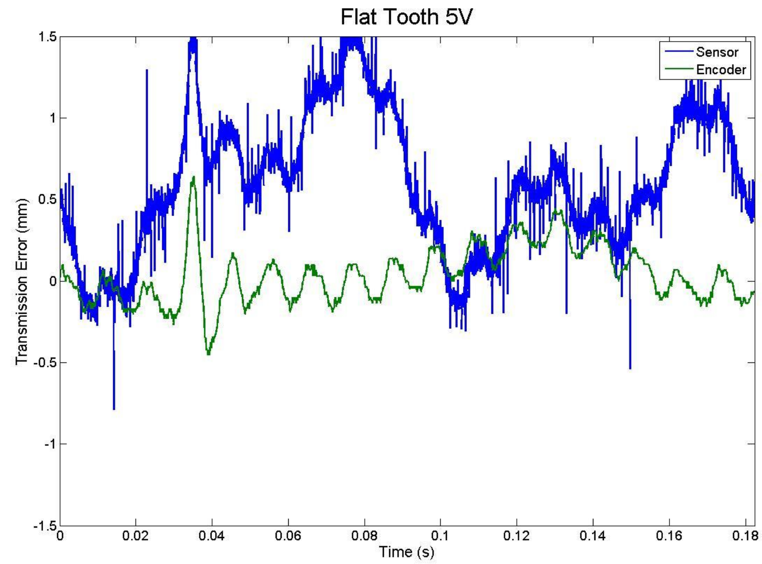

Figure 5.10 - Raw TE for Flat Tooth condition at full load.

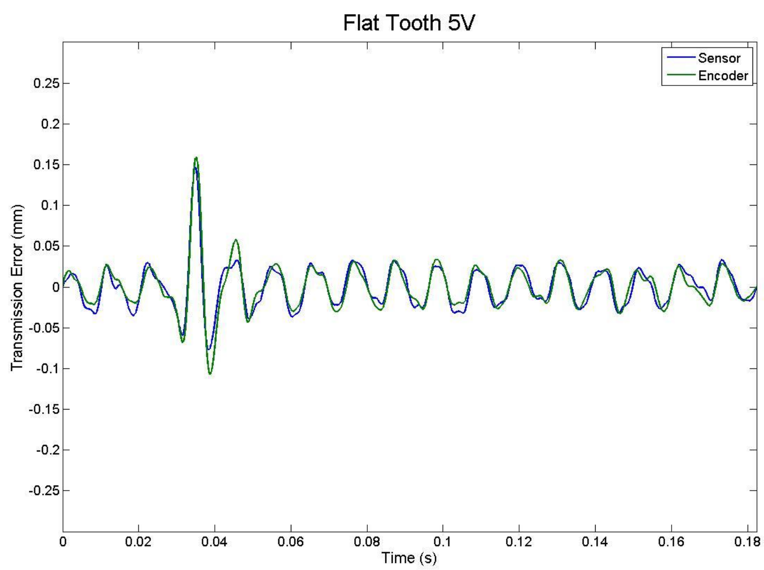

Figure 5.11 - Filtered TE for Flat Tooth condition at full load.

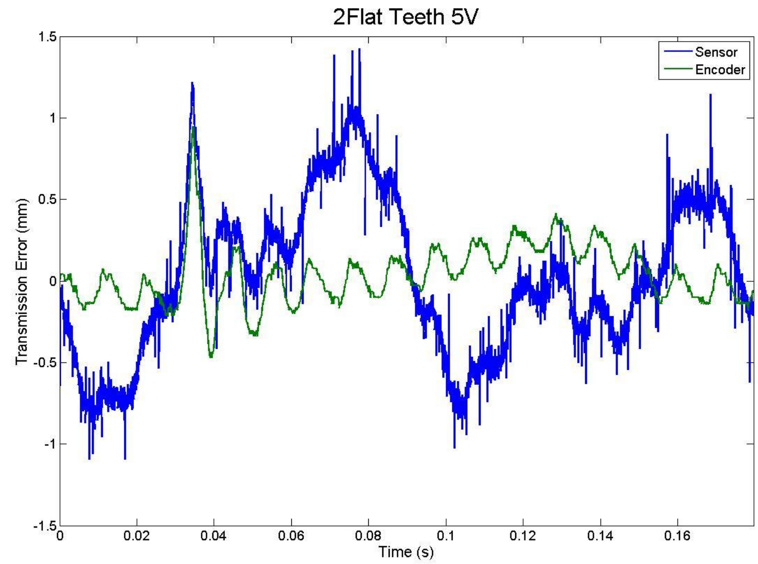

Figure 5.12 - Raw TE for 2 Flat Teeth condition at full load.

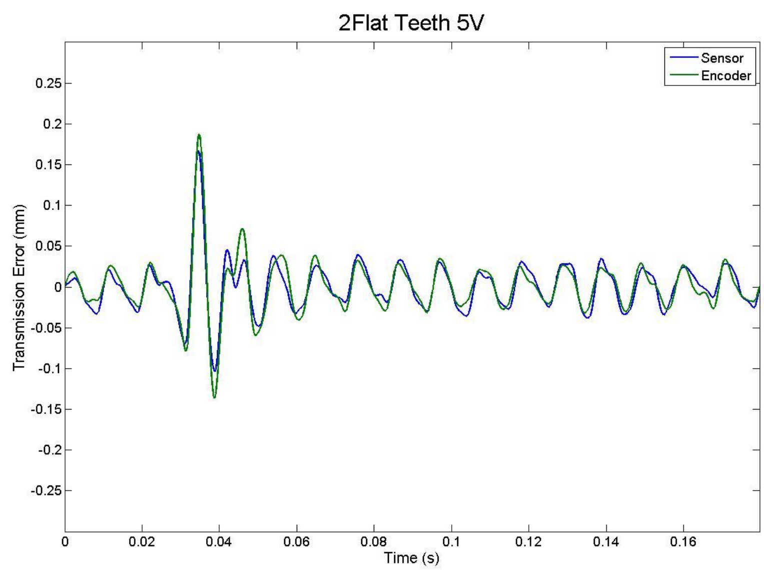

Figure 5.13 - Filtered TE for 2 Flat Teeth condition at full load.

5.4.2 Root Crack Fault

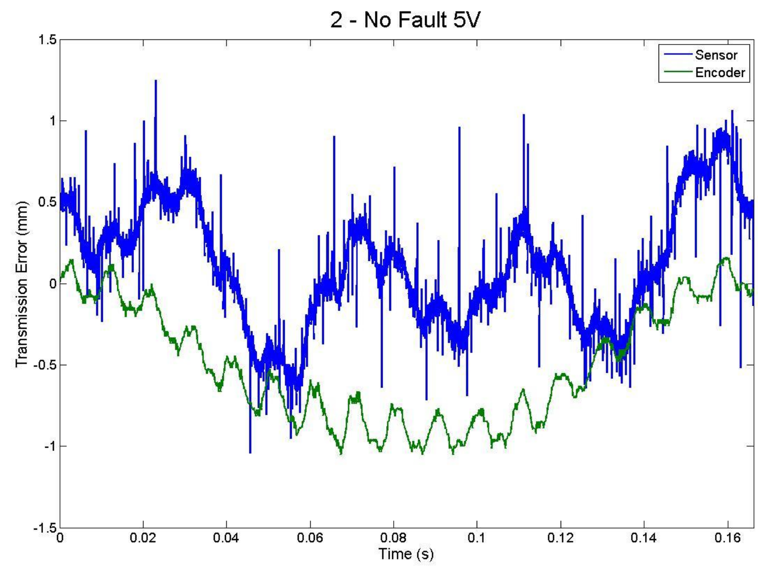

Figure 5.14 - Raw TE for No Fault condition on the second gear set at full load.

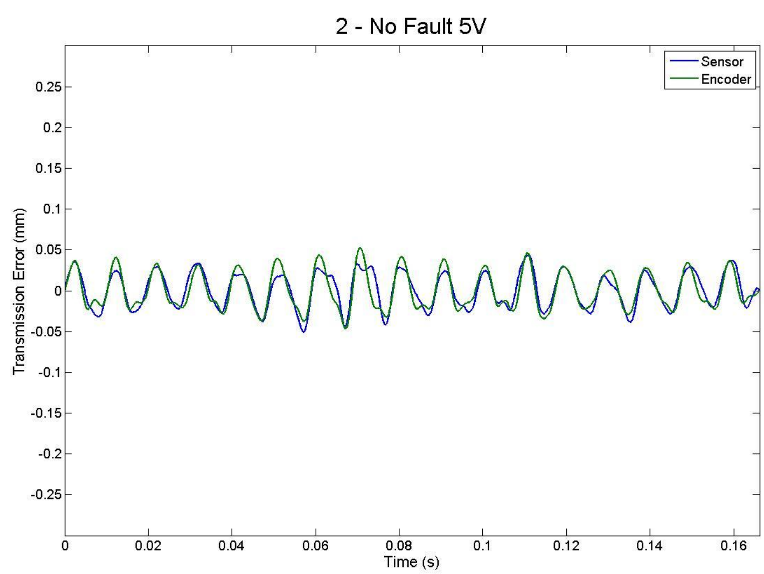

Figure 5.15 – Filtered TE for No Fault condition on the second gear set at full load.

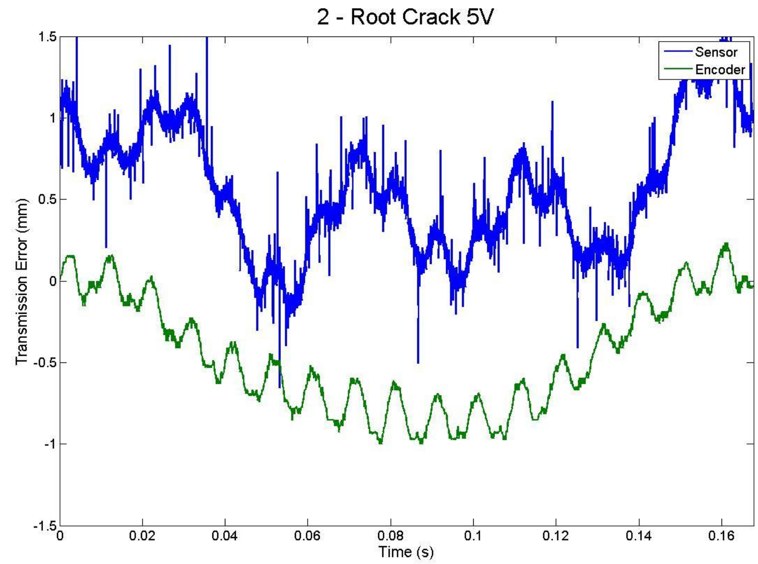

Figure 5.16 - Raw TE for Root Crack condition on the second gear set at full load.

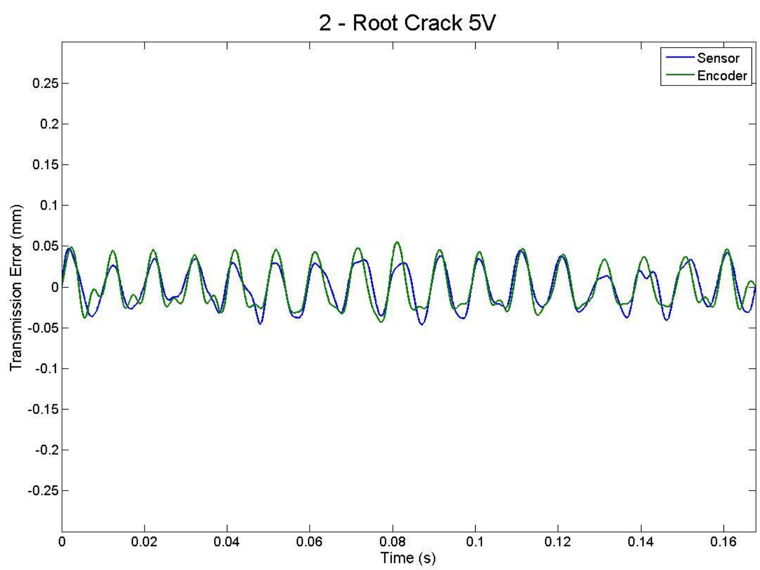

Figure 5.17 - Filtered TE for Root Crack condition on the second gear set at full load.

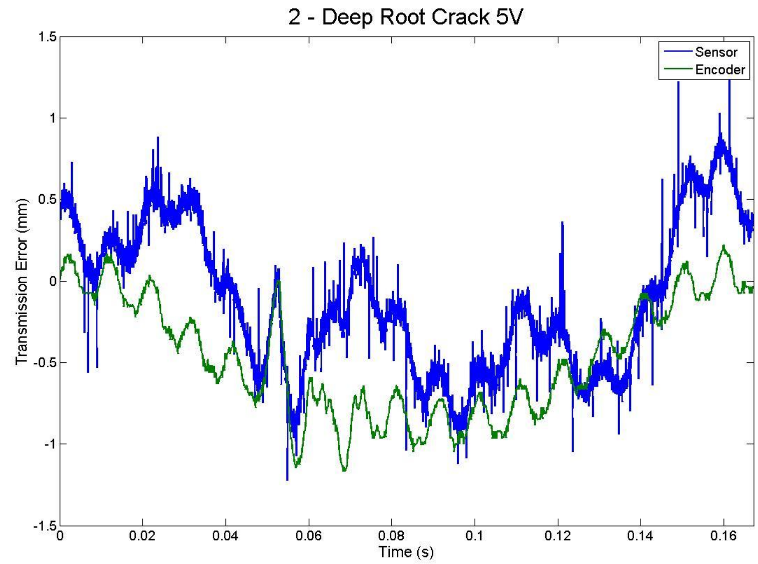

Figure 5.18 - Raw TE for Deep Root Crack condition on the second gear set at full load. Data taken early in test.

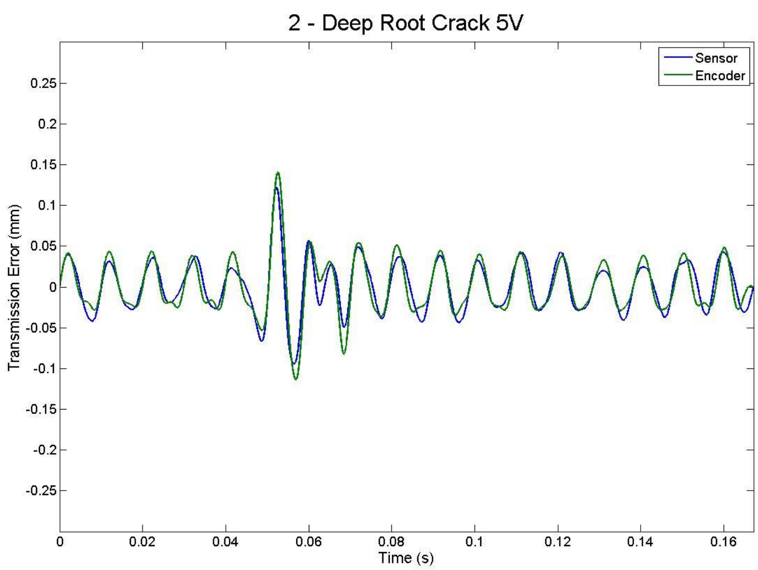

Figure 5.19 – Filtered TE for Deep Root Crack condition on the second gear set at full load. Data taken early in test.

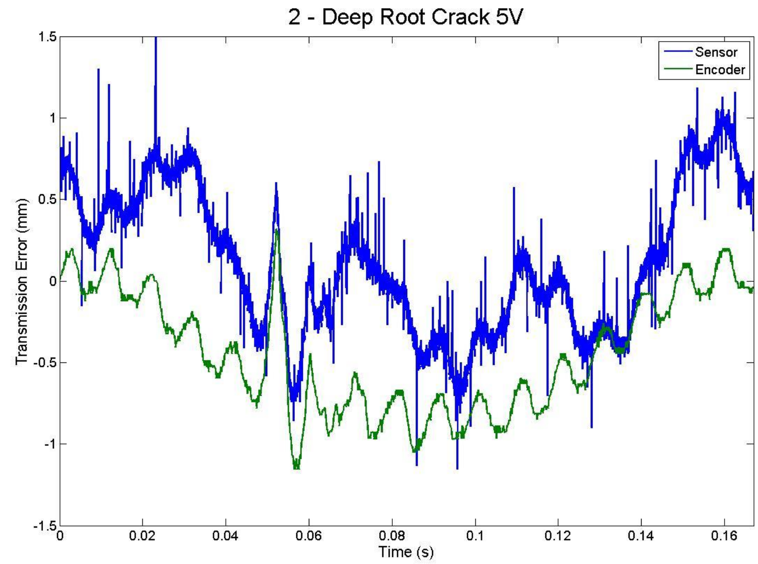

Figure 5.20 - Raw TE for Deep Root Crack condition on the second gear set at full load. Data taken late in test.

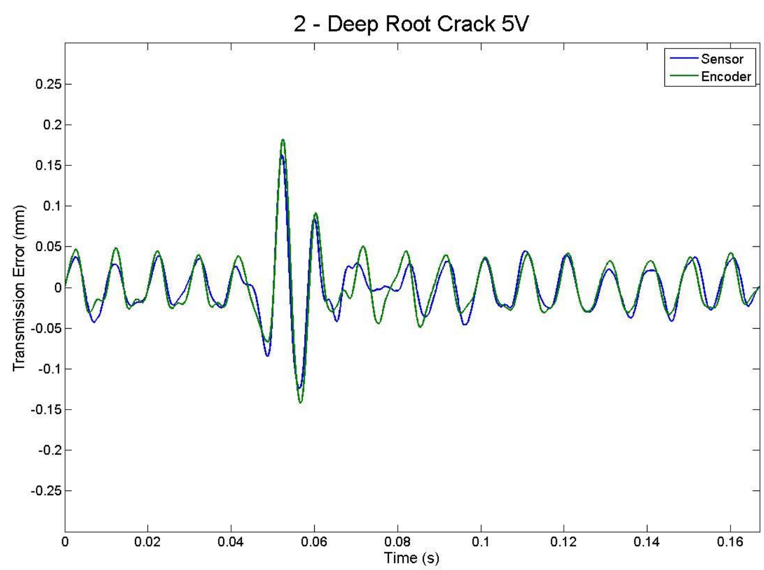

Figure 5.21 – Filtered TE for Deep Root Crack condition on the second gear set at full load. Data taken late in test.

5.5 Characteristic Features

It is observable to the eye from the figures in Section 5.4 and Appendix B that the Transmission Error (TE) changes upon introduction of faults to the gears. Unfortunately, this qualitative analysis is not easily achievable using basic computing. In order to achieve quantitative results in which computer monitoring is applicable, characteristic features must be extracted from the TE which provide an indication of gearbox health. In the case of this study, since the TE is an oscillating signal of varying amplitude, a few typical vibration analysis features were used.

5.5.1 RMS

RMS is an acronym for Root Means Squared (also called quadratic mean). It is used as a measure of amplitude for an oscillating signal as it positively accounts for negative amplitude by squaring and taking the root of signal values. It will fluctuate most when the oscillating portion of the TE for all teeth increases/decreases in magnitude.

5.5.2 Mean

The statistical mean is the cumulative sum of all values. It describes the central location of data.

5.5.3 Kurtosis

Kurtosis is a measurement of datasets ‘peakedness’.

5.5.4 Crest Factor

Crest Factor is a dimensionless quantity which is found by dividing the peak amplitude of a signal by the RMS. It is especially useful in this analysis to detect individual tooth faults with respect to the TE as a whole.

5.6 Characteristic Feature Results over Time

Characteristic features were calculated over the duration of 10 shaft revolutions. For each fault type and loading condition, 100 sets of features were extracted unless limited by gear failure. In most cases, extracted features were uniform over the 100 data sets. For this reason, only graphs which varied over the data collection period will be included in this thesis. The average of the 100 data points was taken for each condition and feature and are included in Section 5.7.

5.6.1 Flat Tooth Fault Aberrations

For the entire running of the first set of plastic gears, there were only two peculiarities which varied over the course of testing. The RMS value during the No Fault condition (Figure 5.22) dipped abruptly under full load.

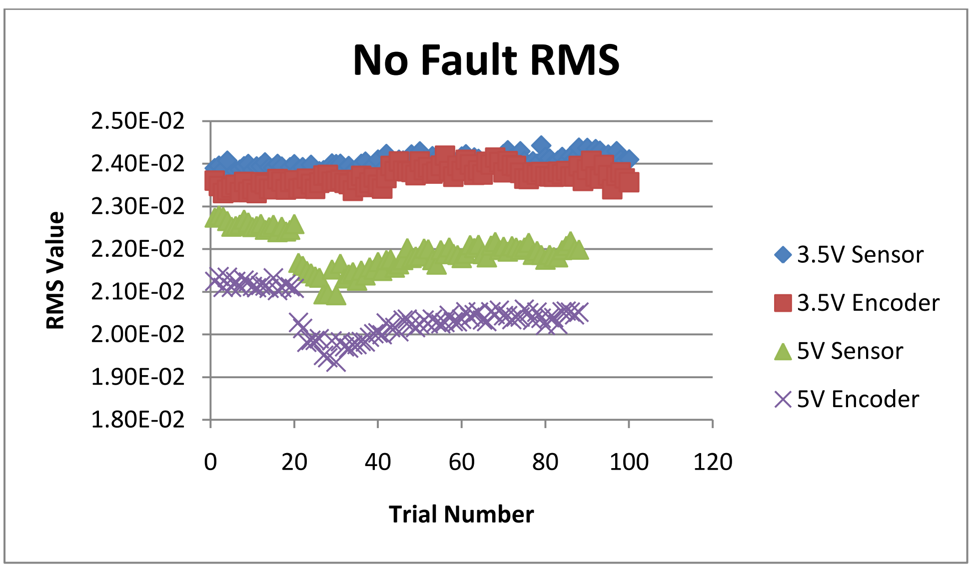

Figure 5.22 - No Fault RMS - Incident during full load test

The RMS during the Flat Tooth condition also gradually changed while overloaded. (see Figure 5.23).

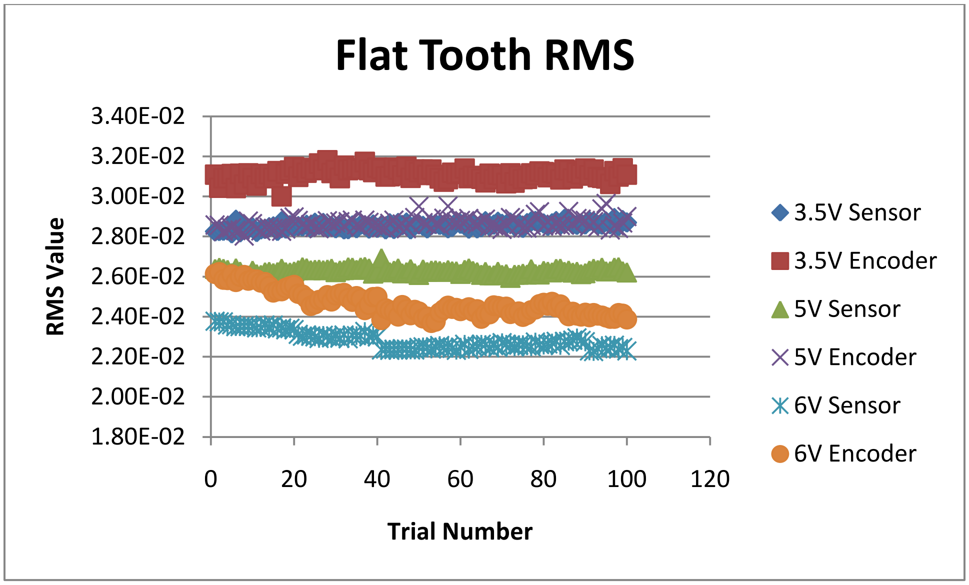

Figure 5.23 - Flat Tooth RMS - Decreased in magnitude during overload condition.

5.6.2 Root Crack Fault Aberrations

The '2 No Fault' fault condition showed RMS 'drift' (Figure 5.24) during data collection at all three load levels, in both positive and negative trends.

More importantly, during the '2 Deep Root Crack' fault condition while fully loaded, the root crack steadily deteriorated until the point of failure. All characteristic features except the mean showed indication of this progression (Figures Figure 5.25 through Figure 5.28).

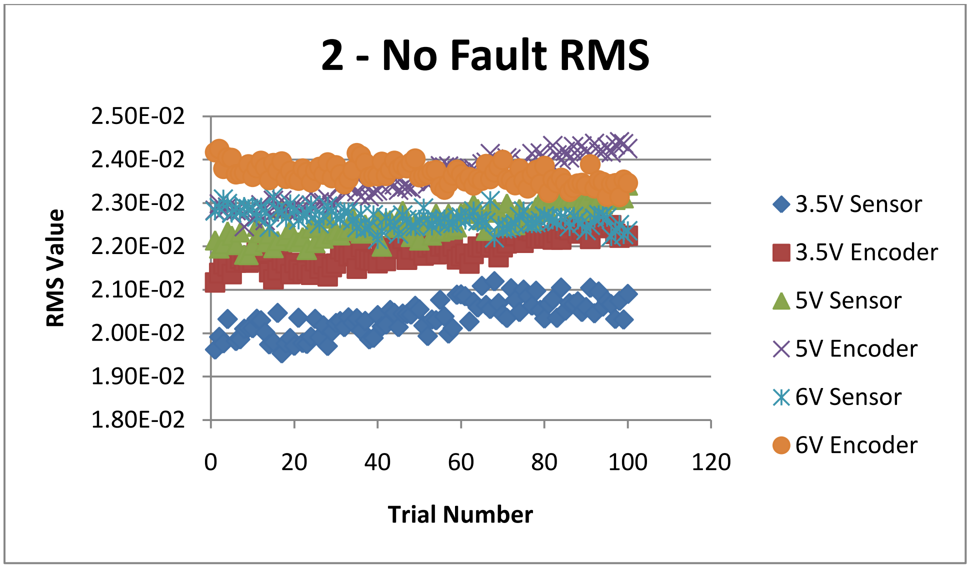

Figure 5.24 - 2 No Fault RMS – Increase in partial and full load, decrease in over load

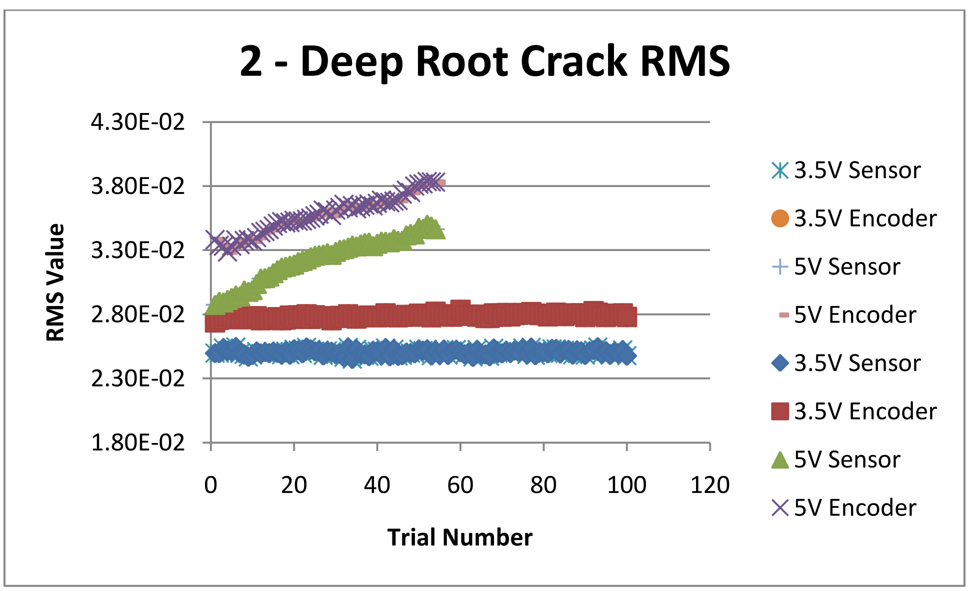

Figure 5.25 - 2 Deep Root Crack RMS - Increasing steadily during failure.

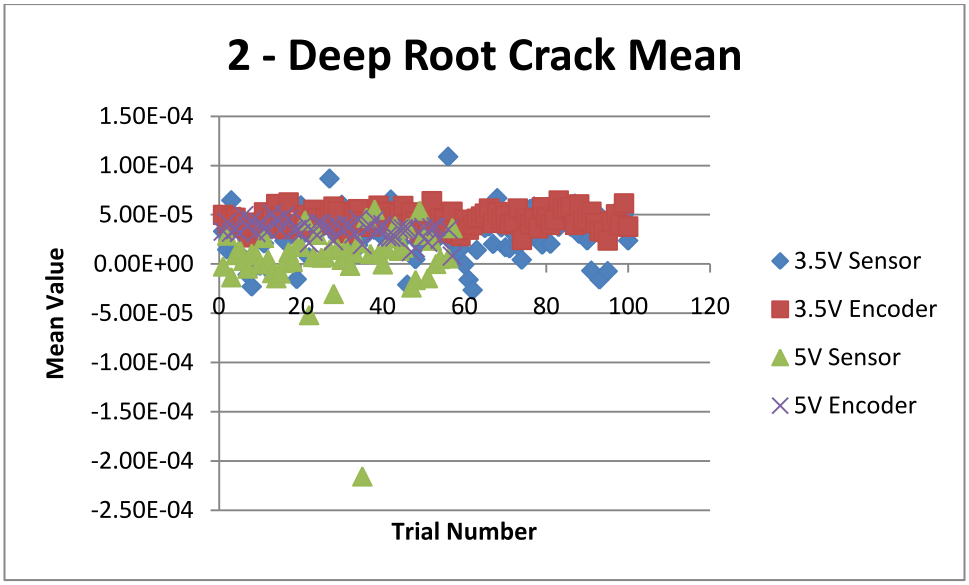

Figure 5.26 - 2 Deep Root Crack Mean – Did not change while failing.

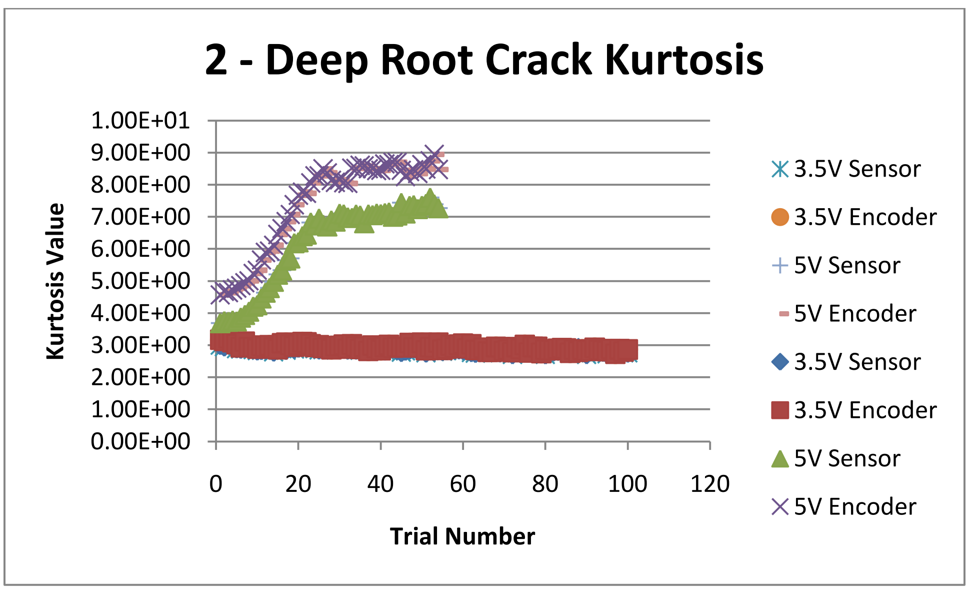

Figure 5.27 - 2 Deep Root Crack Kurtosis - Increased sharply for a time, then gradually increased.

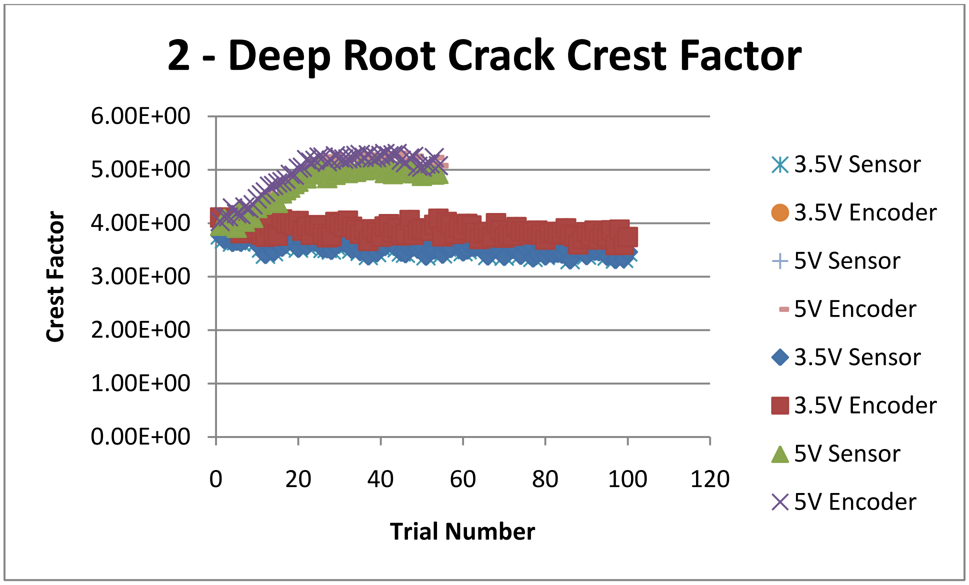

Figure 5.28 - 2 Deep Root Crack Crest Factor - Increased sharply then stabilized.

The 5V medium loading of the 'Deep Root Crack' (as seen in Figures 5.25-5.28) were terminated before the minimum 150 datasets were recorded. This was due to the root crack progressing beyond the induced damage and the gear experiencing catastrophic failure.

5.6.3 Plastic Gear Wear In

Before data collection commenced on the second set of plastic gears, they were run for a period of time to 'break in' the gears. This was carried out to remove surface roughness caused by the resolution of the rapid prototyper. Over this period, data was recorded, and changes to the gear surface were observable as high spots were removed and the gear faces became smooth. The RMS value (Figure 5.29) decreased steadily over this period.

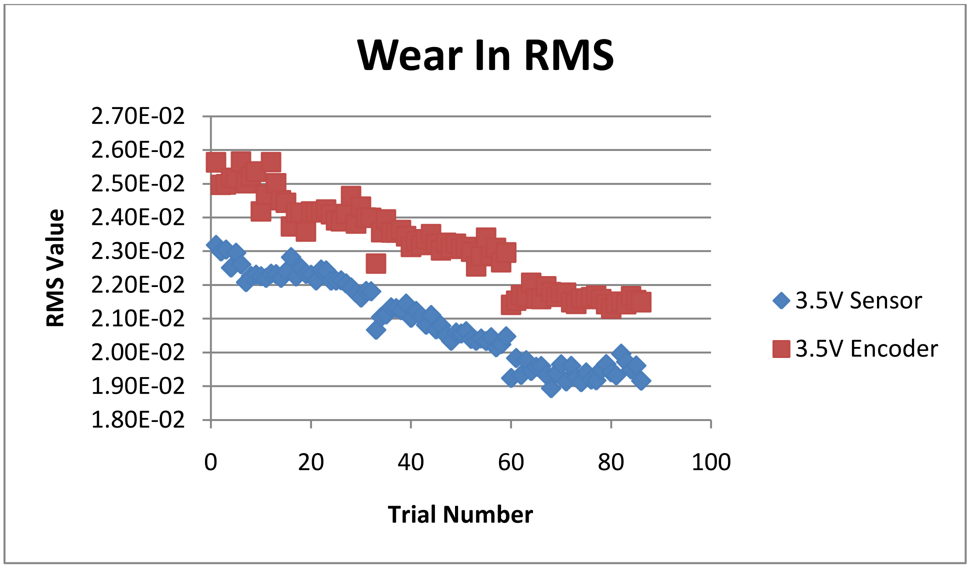

Figure 5.29 - RMS changing over duration of break in period.

5.7 Average Characteristic Feature Results

This section illustrates how the characteristic features varied (on average) with respect to different fault conditions and torque levels. Each data point represents the average value of particular features over the course of 100 data recordings at each combination of load and damage condition.

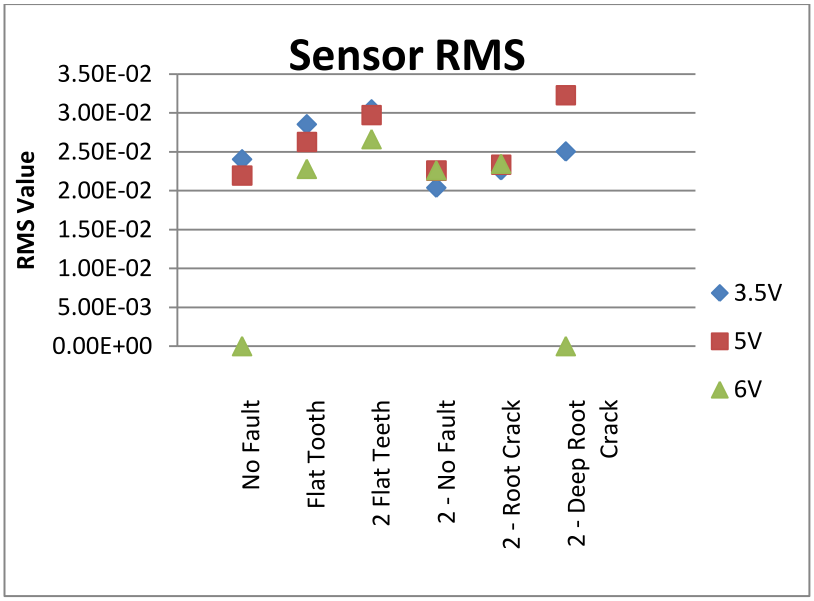

Figure 5.30 - Average RMS value - magnetic sensor.

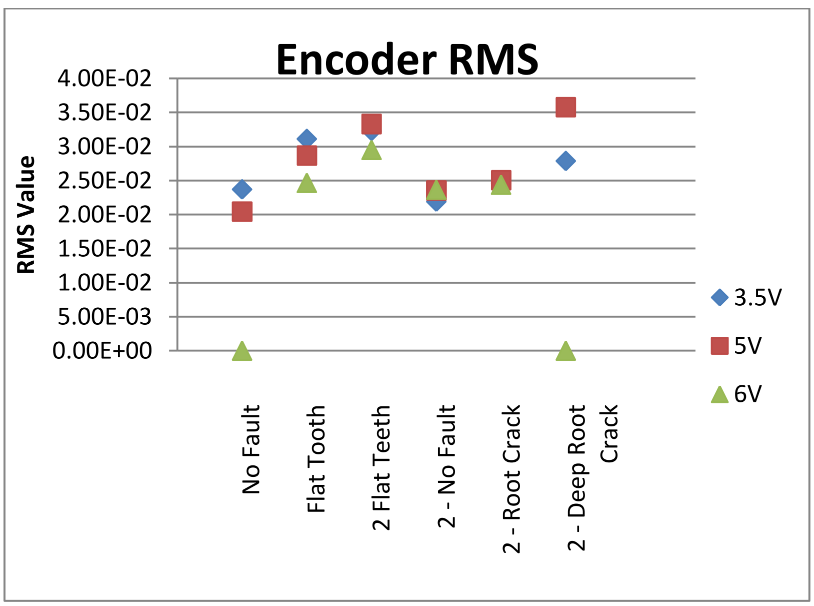

Figure 5.31 - Average RMS value - optical encoders.

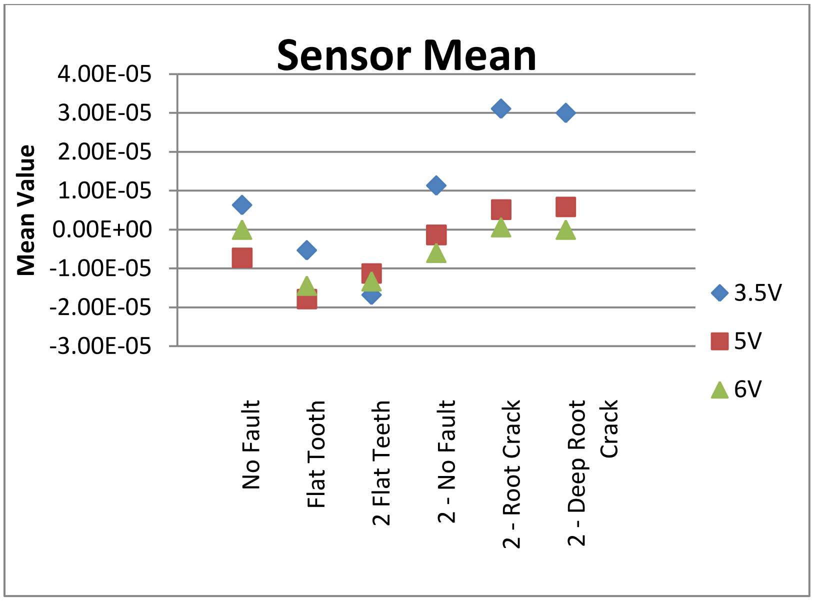

Figure 5.32 - Average Mean value - magnetic sensors.

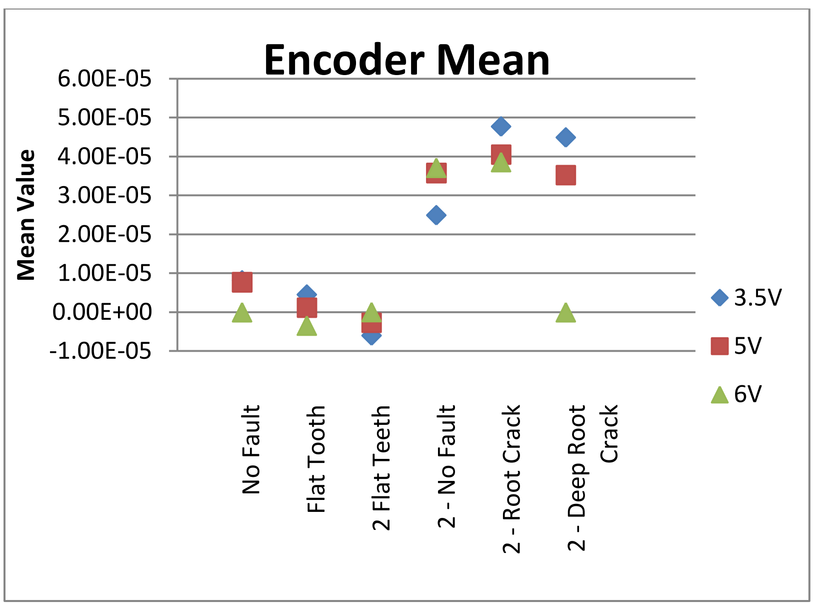

Figure 5.33 - Average Mean value - optical encoders.

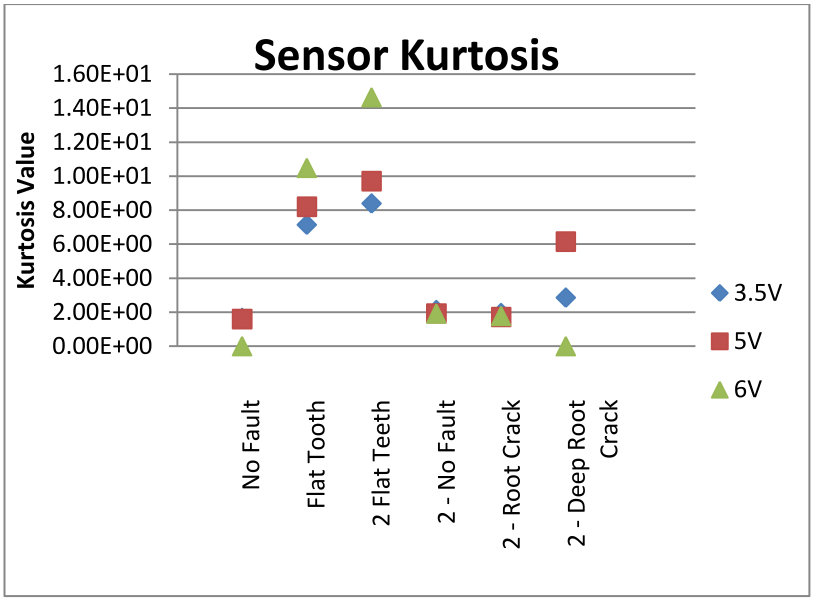

Figure 5.34 - Average Kurtosis value - magnetic sensors.

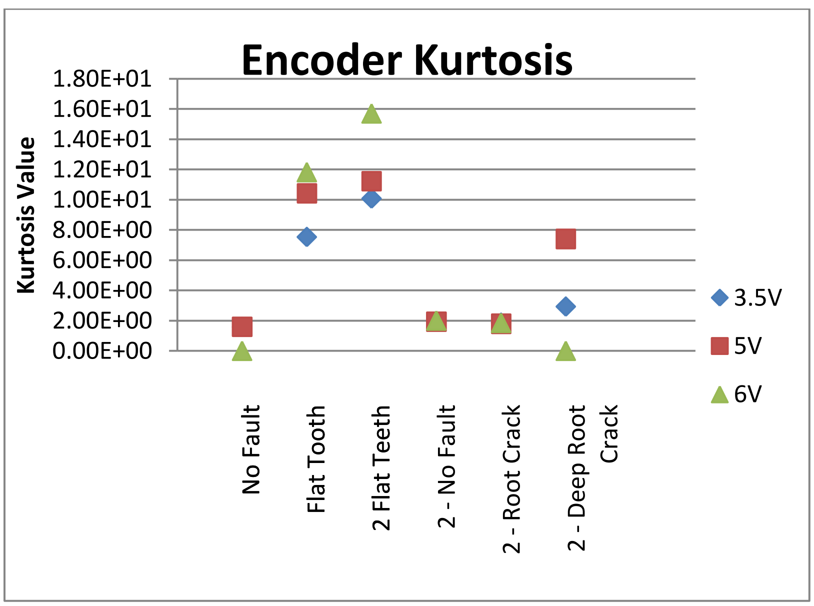

Figure 5.35 - Average Kurtosis value - optical encoders.

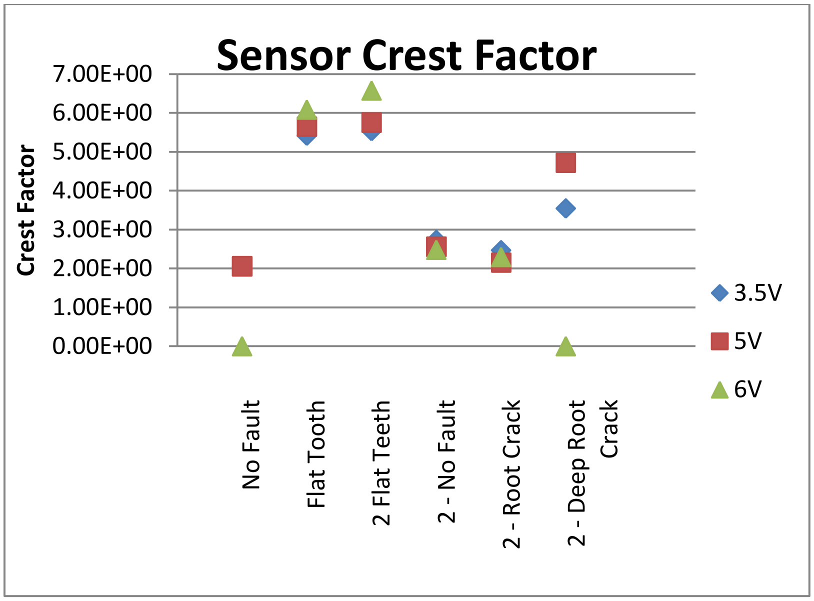

Figure 5.36 - Average Crest Factor - magnetic sensors.

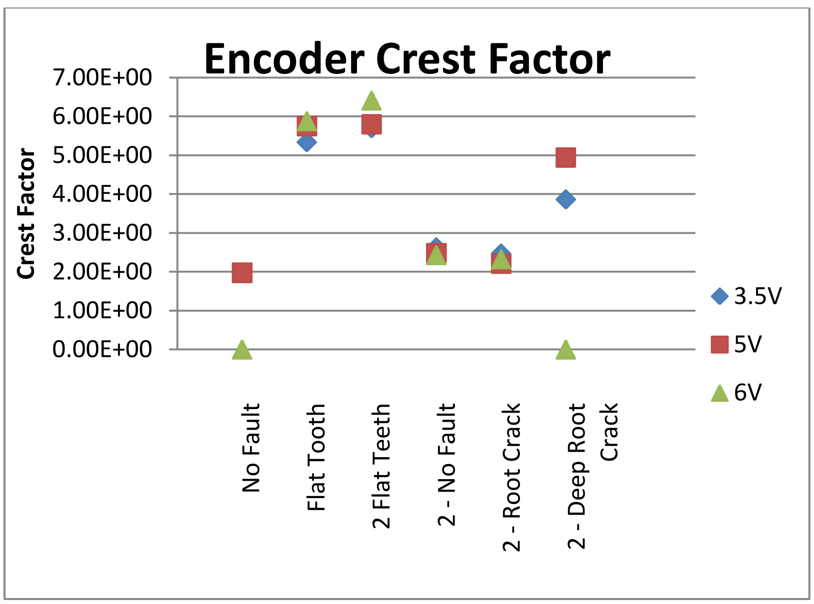

Figure 5.37 - Average Crest Factor - optical encoders.

5.8 Results Conclusion

Chapter 5 has described the evolution of methods used in this thesis to usefully measure and filter Transmission Error (TE) using both magnetic sensors and optical encoders. This TE has in turn been used to observe gearbox dynamics and develop quantifiable parameters to analyze gearbox health.

Chapter 6

Discussion

6.1 Introduction

This chapter is a discussion of the results presented in Chapter 5. It is divided into sections much like Chapter 5 in order to chronologically discuss findings.

6.2 Early Results

Since the steel gears were not of the same size, a gear period method of analysis was established in an effort to properly synchronous average the Transmission Error (TE) (Section 5.2). A sample of early results obtained for TE during testing with steel gears was represented in Figure 5.3. As briefly mentioned, it is largely influenced by an interaction of sensor errors (see the un-calibrated sensor error in Figure 3.7), which individually have a characteristic 4X shaft frequency shape. When the TE was calculated over the duration of a gear period, the two different shaft speeds (each with a 4X frequency error) combined to form a disappointing result in which differences between fault conditions was impossible to discern from close inspection. It was postulated (correctly so) at the time that the gear mesh was being detected (see Figure 5.4 and Figure 5.5) by the magnetic sensors, however proper analysis techniques had not yet been refined. With current techniques, it is believed that the TE can be clearly measured with the magnetic sensors, however lack of data sampled in the same manner as the plastic gear sets makes this impossible to be confirmed at this time.

6.3 Plastic Gear Selection

Nearing the end of the study with steel gears, it was postulated (and has since been confirmed) that the motor and electric brake were not powerful enough to flex steel teeth even if they were individually weakened. Since new gears were to be obtained, a list of desirable criteria was created. A search of the market did not reveal any standouts, so the decision was made to manufacture them in house. The rapid prototyper was used to obtain gears sized to our needs. The spur gear profile was created with large teeth for ease of observing gear mesh. The resolution of the prototyper's printing head was not initially considered, and there were distinct changes to the gear's surface that did not follow the perfect involute. Fortunately, since the teeth are large relative to the resolution limitations (and the material could wear relatively easily), these imperfections ended up not being of consequence. In retrospect, this wear in prior to testing afforded another testing opportunity (Section 5.6.3).

6.4 Gear Fault Severity

The plastic gears were designed to make gear meshing (and subsequently gearbox health) easier to measure. The damage inflicted on the gears was substantially harsher than gradually occurring problems that typically arise in gearboxes. These faults are used as a basic proof of concept to ensure the sensors and encoders can be used to measure TE.

6.5 Filter Size Selection

During the development of the analysis technique used in the latter part of this study, a filter was designed through logic and intuition to remove portions of the signal that were undesirable (sensor errors in Figure 5.6). Previous searches within Matlab had revealed a filtering function described as a zero phase moving window average. Several window widths were experimented with, and the 'wider' window of 200 was selected to remove low frequency fluctuations from the signal resulting in Figure 5.7. This signal was then evaluated using the feature extraction and analysis methods described in Sections 5.5 - 5.7 and found to be discouraging. A reduction of high frequency noise was required. Thus, a similar window average was found by increasing window sizes until the optimum of 120 was reached.

6.6 First Plastic Gear Set

6.6.1 No Fault Condition

The transition from Figure 5.8 to Figure 5.9 indicates how well the previously mentioned filter works for sharpening up TE. The magnetic sensor TE trace matches quite well with the optical encoder trace once filtered, which means the sensor is accurately measuring gearbox dynamics. Raw magnetic sensor TE was calculated without using the optical encoder to calibrate for sensor error. Thus, sensor and encoder results are completely independent. This is a positive result for the magnetic sensor, indicating that it can potentially be used as a replacement for the higher cost optical encoder.

6.6.2 Flat Tooth

The flat tooth defect imparted on the plastic gear (pictured in Figure 4.9) is quite apparent in TE traces (Figure 5.10 and Figure 5.11). Once again, both magnetic sensor and optical encoder are closely matched. The Flat Tooth defect is quite apparent in the raw encoder TE trace when considering Figure 5.10. The raw magnetic sensor trace also indicates this, but it is only noticeable when compared to the encoder trace due to sensor error interfering with the signal. These results show that the magnetic sensor can be used independently from optical encoders once a proper filter is designed.

6.6.3 2 Flat Teeth

Similar to the Flat Tooth condition, Figure 5.12 and Figure 5.13 show the effectiveness of filtering methods used in this thesis. Sensor and encoder TE traces shadow each other closely, and indicated an error that was greater in magnitude than the Flat Tooth condition. In addition to this, there is a bounce at the next expected tooth mesh, which indicates that the 2 Flat Teeth fault not only affected the damaged teeth, but also that gearbox dynamics for other meshing teeth were changed.

6.7 Second Plastic Gear Set

In all cases for the second plastic gear set, the raw optical encoder signal shows a large negative (see Figure 5.14,Figure 5.16,Figure 5.18, Figure 5.20) trend which is unknown and unexpected. It may be the result of eccentric gears or misalignment, but the low speed portion of the filter was able to remove it, as the filtered TE traces were fine.

6.7.1 No Fault Condition

The same analysis detailed in Section 6.6.1 applies for the second set of plastic gears. Filtered magnetic sensor and optical encoder TE traces (Figure 5.15) oscillated regularly without indication of individually damaged teeth as expected, adding to the sensor's reliability to accurately detect gear mesh and faults independently of encoders.

6.7.2 Initial Root Crack

As seen in Figure 5.17, the root crack goes undetected by both types of position sensor. Even the overload condition (found in Appendix B) did not cause measurable tooth deflection. Since the root crack was measureable upon further damage, the location of the weakened tooth on the gear was pinpointed. If the tooth was flexing, the peak corresponding to 0.05 seconds should vary with respect to its neighboring teeth. This is not the case, which is why it can be concluded that the gear was rigid enough to resist tooth bending despite being weakened at the root (for the initial damage imparted).

6.7.3 Deep Root Crack

Consulting with Appendix B, the TE trace for the partial load level exhibited tooth flexion. Similar to Section 6.6.3, the fault is visible in both raw TE traces (Figure 5.18), though the encoder trace is needed as a reference identify which spike is the fault. Once filtered (Figure 5.19), the close conformity between sensor and encoder TE indicated a localized fault (the root crack). It appears similar to the flat tooth fault because the amplitude of one peak increases with respect to the others, with almost no other deviation.

Over the course of the full load test, the root crack progressed (also discussed in Section 6.8.2, result found in Figure 5.21). As expected, the magnitude of the individual peak increased (by approximately 20%). This demonstrates the effectiveness of the method used to calculate TE, as well as the sensitivity of the sensors and encoders (more on this in Section 6.8.2)

6.8 Characteristic Feature Indicators over Time

6.8.1 Unexpected Results

As mentioned in Section 5.6, features extracted from sequential data sets were monitored to observe changes over time. For the most part, the indicators remained constant for the duration of data collection, indicating the gears were relatively stable and unchanging. Incidences where the feature did not remain constant were included as part of the results.

RMS over time is expected to decrease as the gears wear in (confirmed by Figure 5.29). This is why Figure 5.22 (No Fault) is unexpected. The full load condition suddenly changed value, decreased for a period, and then increased. One possible explanation for this might be thermal effects. Despite forced convection cooling, the motor and brake would heat up to uncomfortable levels, so caution was exercised and testing would stop until they cooled. This is not the only example of interrupted testing. It is also possible that trials concluded for the day and resumed the following morning when temperatures were cooler.

The change in the overload RMS in Figure 5.23 is perhaps more explainable. Over the course of testing, its value slowly but steadily decreased by 10%. It is likely that the heavier load was able to further break in the gear for smoother operation.

The last unexpected outlier of data in this section is Figure 5.24. The partial load shown here chronologically followed the 'Wear In' period (Figure 5.29, in which RMS was decreasing). At the conclusion of 'wearing in' the gears, the Sensor RMS appeared to stabilize at approximately 1.95×10^{-2}. Upon continuation of testing, the Sensor RMS was approximately the same, but it increased steadily over the course of data collection.

6.8.2 Progression of the Deep Root Crack to Failure

For all of the characteristic features, the partial load on the '2 - Deep Root Crack' remains steady, indicating the fault was not progressing during this testing. Increasing brake torque input to full load incited changes (generally) across the board. Figure 5.25 shows how the RMS increased steadily as the fault progressed. The Kurtosis (Figure 5.27) on the other hand increased sharply until approximately the 25th sample, and then continued increasing at a reduced pace. This, combined with the behavior of the Crest Factor (Figure 5.28) signifies the fault progressed rapidly for a period of time and then catastrophically snapped in some manner (around the 25th sample). After that, the tooth was rooted in place by a small piece of material. When the gearbox was halted mid-run, the tooth was able to freely wiggle. At the slightest pressure though, the tooth became dislodged permanently. When the gearbox was still running, the tooth was able to move freely back and forth, avoiding contact stresses and allowing neighboring teeth to shoulder the load.

6.8.3 Wear In Period RMS

Although previously referenced several times in this section, it is important to note the significance of RMS as it pertains to changes affecting all gear teeth simultaneously. The RMS continually decreases in Figure 5.29 until it stabilizes at its worn in state.

6.9 Characteristic Feature Summary

6.9.1 RMS

As measured by optical encoders and magnetic sensors, RMS values closely agree (Figure 5.30 and Figure 5.31). RMS increased in magnitude as more severe faults were introduced. Except for the case where the fault was progressing to failure (2 – Deep Root Crack 5V), RMS values tended to decrease with increased load, indicating a net reduction in the periodic signal of the TE. This could mean the gears vibrated less as load was increased. Decreasing RMS over time (Wear In) demonstrated the method’s sensitivity to changing dynamics, as well as confirming that the plastic gears needed to break in prior to testing.

6.9.2 Mean

Mean values did not corroborate well between magnetic sensors and optical encoders. This is inconsequential though, as they appear to be meaningless for fault detection of this nature. This is rational, though, since the filter was used to reduce low speed error and centre the signal about zero.

6.9.3 Kurtosis

Kurtosis results matched up well for magnetic sensor and optical encoders. Figure 5.34 and Figure 5.35 look similar in shape and magnitude. As faults to individual teeth increased, the peakedness of the signal did so as well, with kurtosis scores ranging greatly for the flat tooth conditions. At faulty conditions, the Kurtosis values also seems to separate more when the load was varied, as it is more sensitive to increases in localized faults. The Kurtosis values did not change during Wear In. This makes sense as there was a net 'settling in' for each tooth meshing pair, presumably affecting all peaks equally.

6.9.4 Crest Factor

In a similar manner as Kurtosis, the Crest Factor picked up on the flat tooth faults quite strongly. It decreased very slightly when the initial root crack was introduced. This is due to the peak of the signal remaining unchanged, while the RMS climbed slightly (recall the definition of Crest Factor in Section 5.5.4).

6.10 Value of Changing Results

It was fortunate that the fault progressed during full load testing of the Deep Root Crack. This allowed the encoders and sensors (as well as the analysis method) to exhibit sensitivity to progressive change rather than abrupt changes (Flat Tooth to 2 Flat Teeth). Similar value is placed on the wear in results. Machine condition monitoring is a process intended to detect changes in machine dynamics which can forewarn part failure.

6.11 Conclusion

This chapter has discussed the importance of the variety of results presented in Chapter 5. The measurement of Transmission Error by the magnetic sensors (when filtered properly) was compared to the optical encoders, which was found to be the same. Feature extraction methods revealed that different parameters can quantify different aspects of Transmission Error (and thus gearbox dynamics).

Chapter 7

Conclusion and Future Work

It has been proven that, provided correct filtering, non-contact magnetic rotational position sensors can measure Transmission Error as effectively as optical encoders. Both sensing devices were used to generate TE traces clearly showing gear mesh. Furthermore, these TE traces showed individual tooth faults such as damaged gear teeth and root cracks.

In order to quantify these results, feature extraction using RMS, Kurtosis, Crest Factor, and Mean as parameters were employed. RMS was excellent at providing insight on changes occurring on all teeth simultaneously. An example of this was the strong correlation during the 'Wear In' process. Both Kurtosis and Crest Factor were used as strong indicators of localized faults occurring on individual teeth. They increased dramatically as tooth damage increased. The Mean value did not bear meaningful results in this area due to the nature of the signal and filtering process.

These parameters also showed sensitivity to slowly changing dynamics while a root crack grew progressively to the point of failure. Traits like these are highly desirable in machine condition monitoring as they are used to reveal the onset of catastrophic failure.

An area of opportunity for future work would be to monitor a gearbox from break in to failure without external influences. Recording regularly spaced data samples using the current data collection procedure from start up to eventual failure would further identify useful characteristic features obtainable from the Transmission Error trace. Over time, a library of fault conditions and incipient failure indicators could be amassed.

Another opportunity for future work would be to re-examine the steel gears used at the beginning of this study. Using the updated data acquisition method and modifying filter values would results in increased clarity of the TE traces.

Ultimately, these inexpensive non-contact rotational position encoders were used to accurately detect and measure Transmission Error, providing a means to quantify and qualify gearbox health.

Appendix A

Magnetic Sensor Response at Different Orientations

This appendix is included to document the variety of alignments and orientations possible with the non-contact rotation position sensor. This work was undertaken to investigate other suitable orientations should space requirements interfere with the default position of the axially centered sensor. The thinking behind this work was that the sensor might be able to resolve the rotating magnetic field in the same manner as normal while oriented differently. Two magnet configurations were used for testing.

The first magnet was labeled 35mm MMG XY. It is a diametrically polarized magnet similar to the magnet used in this thesis, however its diameter is greater. This sized magnet was useful for testing as it allowed for greater sensitivity to sensor placement axially offset near its outer diameter.

The second magnet used in testing was a ring magnet. It is diametrically polarized in the same manner as previously mentioned, however the center has been milled out after polarization. This style of magnet was used to test the viability of radial sensing rotational position if the end of shaft was unavailable.

Different orientations were tested on a custom built rig at Litens. A small electric motor rotated a shaft upon which the two position sensing devices were mounted (a 360 pulse per revolution optical encoder and a removable mount for the magnets). The sensing head for the non-contact magnetic sensor was held in place by an XY table that also allowed rotation. The encoder and magnetic position sensor were hooked up to a computer to resolve position data for each device. As previously mentioned in Section 3.6, there are several steps required to go from sensor output (sinusoids) to position (normalizing, arctan).

Data collection consisted of noting approximate magnitudes of the sinusoids, as well as the shape of the final signal. The magnitude of the sinusoids is important as it gives a preliminary indication of sensor resolution at that orientation. It is desirable for each sinusoid to be almost saturated (in this case it was 7000 units), as the arctan function will deliver a higher resolution. When one or both sinusoids had decreased amplitude, sensor resolution decreases as well. The shape of the signal (as compared to the 360 PPR encoder) indicated sensor accuracy.

In all diagrams, the magnet is colored medium grey, and the sensing head is shaded darker grey.

Magnet: 35 mm MMG XY - Axial Sensor Alignment

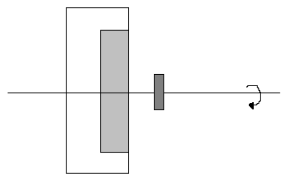

Figure A1 – Sensor positioned on axis of rotation

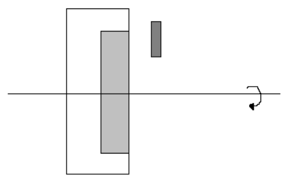

Figure A2 – Sensor positioned below edge of magnet

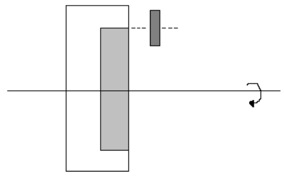

Figure A3 – Sensor positioned adjacent to magnet edge

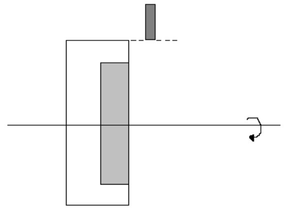

Figure A4 – Sensor positioned at the edge of the assembly

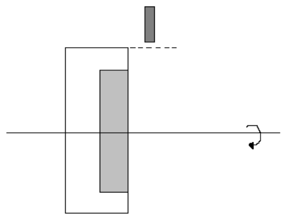

Figure A5 – Sensor positioned beyond assembly

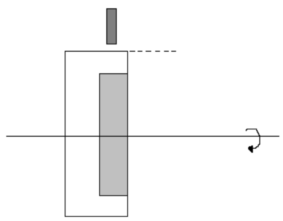

Figure A6 – Sensor position radial to magnet

Figure	Sine Amplitude	Cos Amplitude	Sensor Position Shape
1	7000	7000	normal
2	7000	2000	non-linear
3	6000	0	square wave
4	4500	4500	normal
5	2000	3700	reversed direction
6	2200	5000	reversed direction

Magnet: 35 mm MMG XY - 45° Sensor Alignment

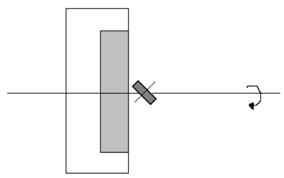

Figure A7 – Sensor positioned on axis of rotation

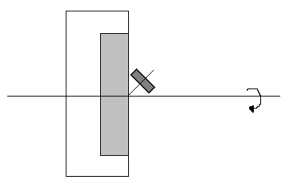

Figure A8 – Sensor positioned with normal projecting on axis of rotation at the magnet face

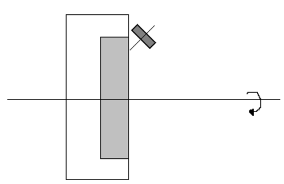

Figure A9 – Sensor positioned to project halfway along the radius of magnet

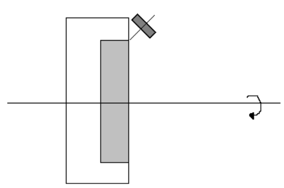

Figure A10 – Sensor positioned to project normal on magnet edge

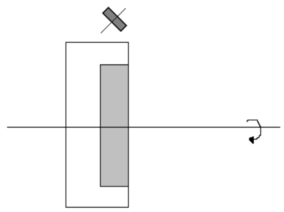

Figure A11 – Sensor positioned radial to magnet

Figure	Sine Amplitude	Cos Amplitude	Sensor Position Shape
7	6800	5200	normal
8	6800	6800	normal
9	5100	6100	normal
10	3000	600	non-linear
11	3200	7800	reversed direction

Magnet: 35 mm MMG XY - Tangential Sensor Alignment

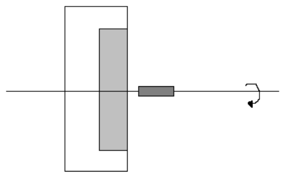

Figure A12 – Sensor positioned along axis of rotation

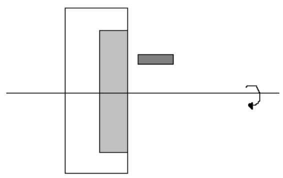

Figure A13 – Sensor positioned between center and radius

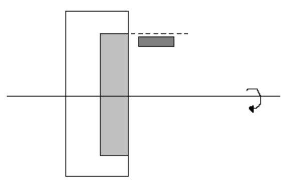

Figure A14 – Sensor positioned within magnet edge

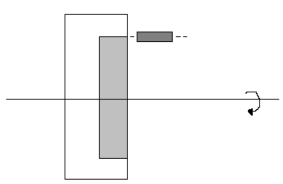

Figure A15 – Sensor positioned at outside edge of magnet

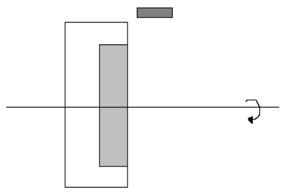

Figure A16 – Sensor positioned outside of magnet face

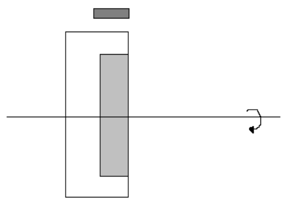

Figure A17 – Sensor positioned radial to magnet

Figure	Sine Amplitude	Cos Amplitude	Sensor Position Shape
12	6000	500	non-linear
13	5800	4000	normal
14	5600	5600	normal
15	3500	6500	normal
16	2200	4200	non-linear
17	4100	2000	reversed direction

Ring Magnet - Axial Sensor Alignment

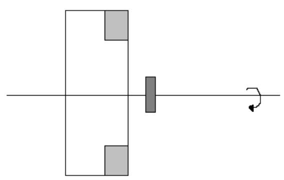

Figure A18 – Sensor positioned on axis of rotation

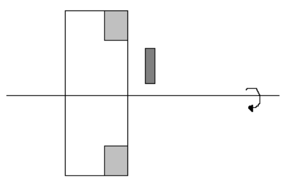

Figure A19 – Sensor positioned off rotational axis inside of ring magnet

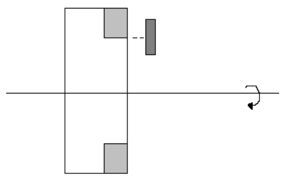

Figure A20 – Sensor positioned on inside edge of magnet

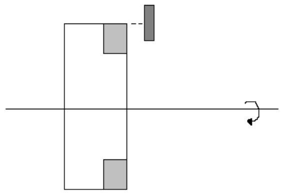

Figure A21 – Sensor positioned on outer ring of magnet

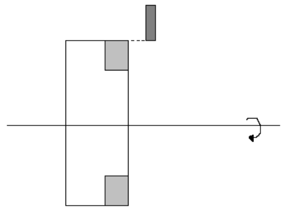

Figure A22 – Sensor positioned with edge of chip aligned with outer magnet edge

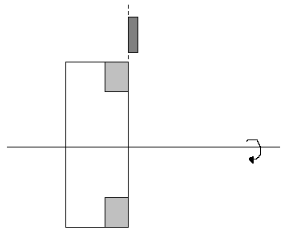

Figure A23 – Sensor positioned with edge adjacent to face plane

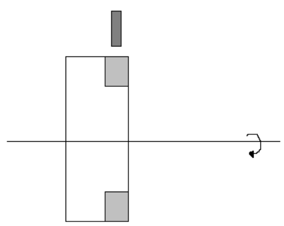

Figure A24 – Sensor positioned radial to magnet

Figure	Sine Amplitude	Cos Amplitude	Comments
18	2500	2500	Sine reversed, equivalent amplitude, linear shape
19	0	2000	Cos distorted, square wave
20	7500	0	Sine big, no cos, square wave
21	6000	6000	Reversed direction, sine > cos, sine DC offset, non-linear
22	0	6000	Sine DC offset, equivalent amplitude
23	7500	3000	Normal
24	7300	3000	Normal

Ring Magnet - Tangential Sensor Alignment

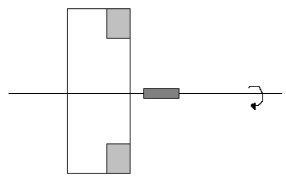

Figure A25 – Sensor positioned on axis of rotation

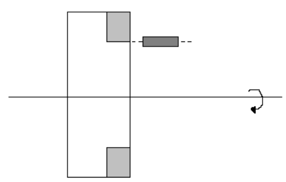

Figure A26 – Sensor positioned on inner edge of ring magnet

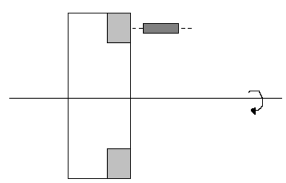

Figure A27 – Sensor positioned in middle of ring magnet thickness

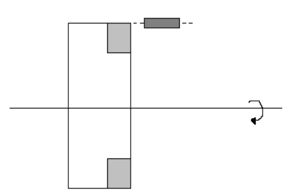

Figure A28 – Sensor positioned at outer edge of ring magnet

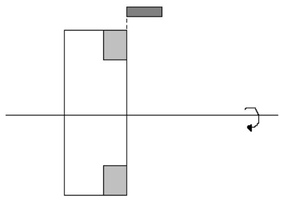

Figure A29 – Sensor positioned outside and adjacent to ring magnet face

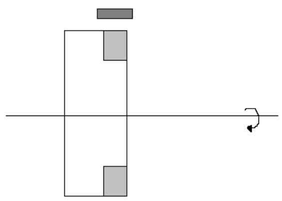

Figure A30 – Sensor positioned radial to ring magnet

Figure	Sine Amplitude	Cos Amplitude	Comments
25	800	0	Poor amplitude and shape
26	2200	1600	Sine and cos have distortion
27	3000	3000	Sine is distorted, DC offset
28	6200	3300	Sine has DC offset, linearity problems, reversed direction
29	7600	3800	Linearity problems, reversed direction
30	7500	8000	Sine has DC offset, linearity problems, reversed direction

Sensor Orientation Conclusions

It was decided at the conclusion of response mapping that a sensor orientation outside the diameter of the shaft would be pursued. Upon closer inspection of relevant orientations (Figures 5, 6, 11, 17, 23, 24, 29, 30), the MMG magnet and tangential orientation for the ring magnet was discounted due to poor performance.

Further trials with the ring magnet showed that the amplitude of sine and cosine waves could not be used to fully exemplify the position signal. In several cases, the waves would change from a sinusoid into an oscillating signal that was sharper and skinnier around the peaks (not true sinusoids), which result in a position signal that behaved non-linearly for constant speeds.

This extra analysis found the radial sensor position depicted in Figure A24 to be the best for linearity with most signal resolution. The amplitude of the cosine signal was less than half of the sine, however they were both properly shaped to allow for scaling. This means there is some resolution loss in position signal, however a relatively reliable position can be obtained.

Using this orientation, tests using the existing code programmed for the axial button magnet showed preliminary accuracy to be 0.4°, whereas the button magnet was 0.1°. Another magnet/holder set-up was not available to be tested, so it is unknown whether mechanical problems relating to oscillation and vibration of the magnet was responsible for this decrease in accuracy.

Appendix B

Full Transmission Error Results

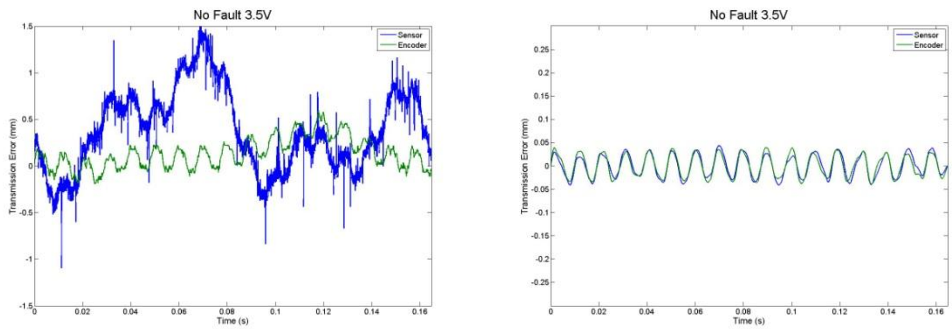

No Fault 3.5V

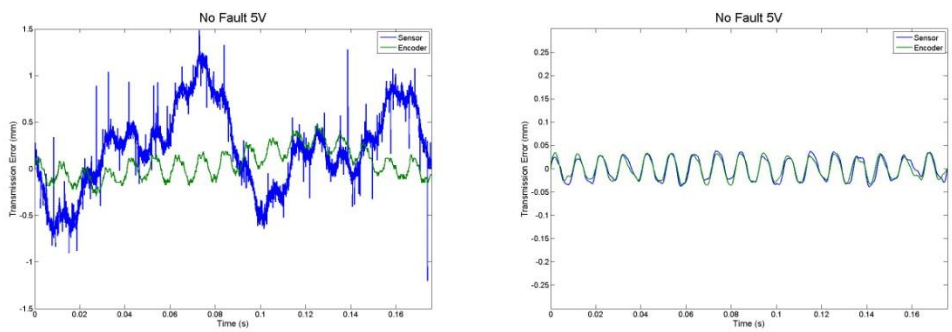

No Fault 5V

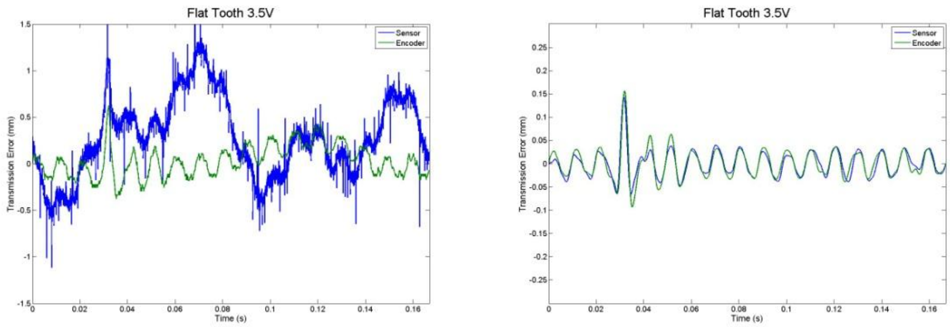

Flat Tooth 3.5V

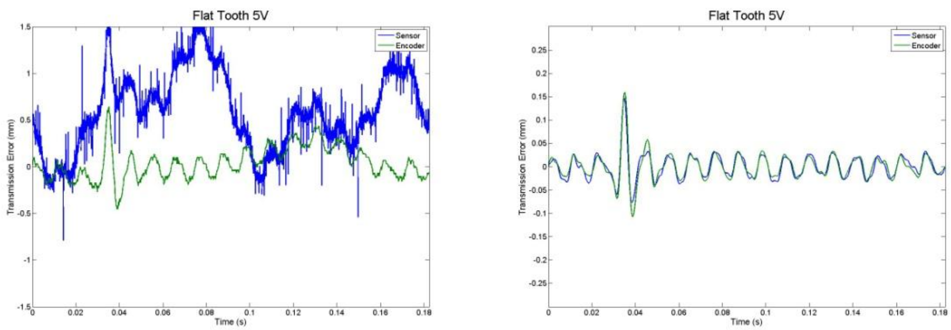

Flat Tooth 5V

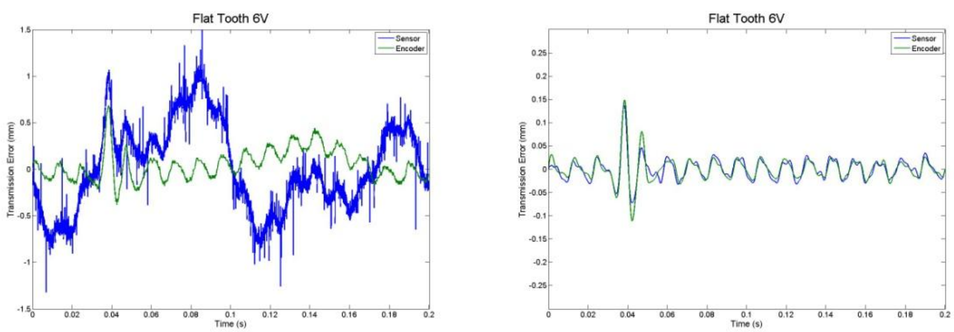

Flat Tooth 6V

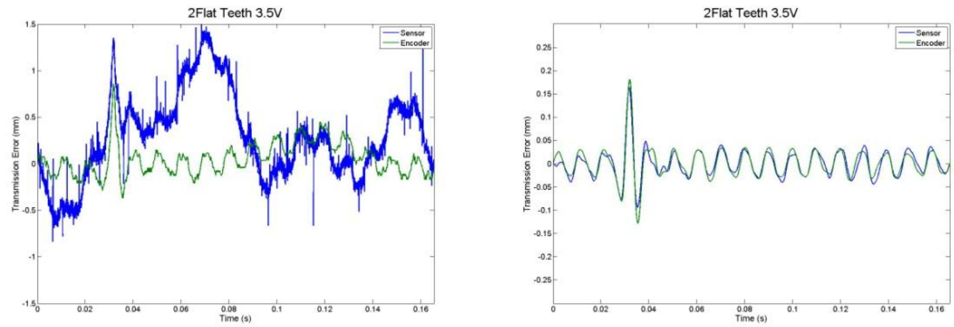

2 Flat Teeth 3.5V

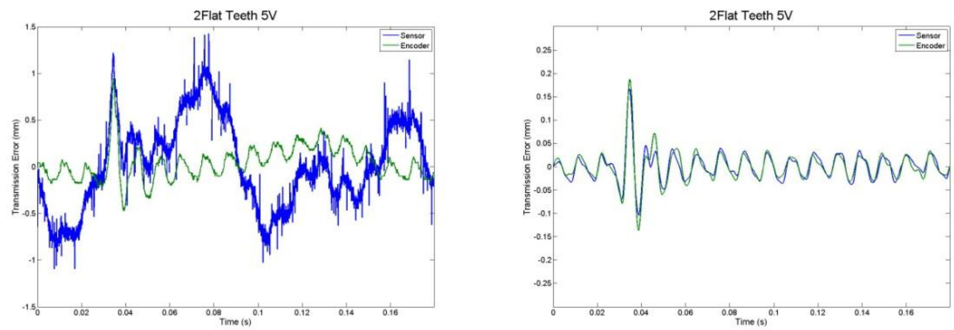

2 Flat Teeth 5V

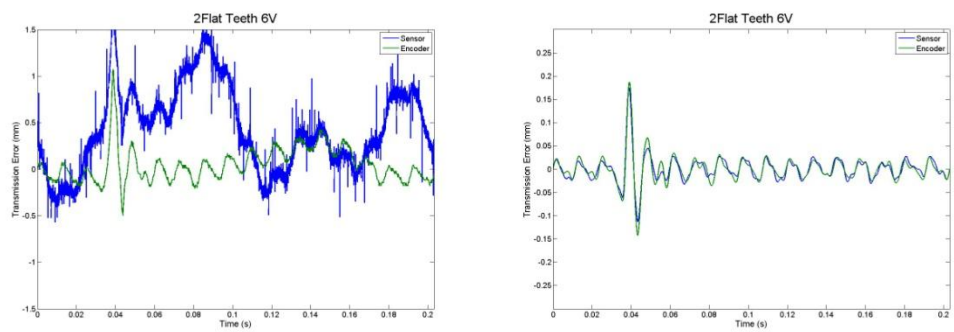

2 Flat Teeth 6V

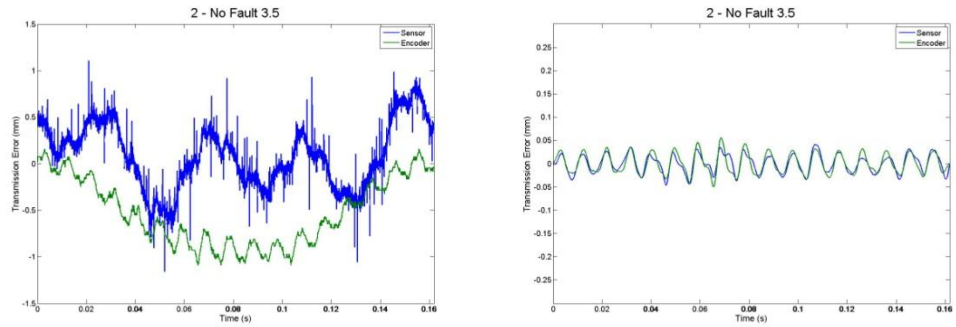

2 – No Fault 3.5V

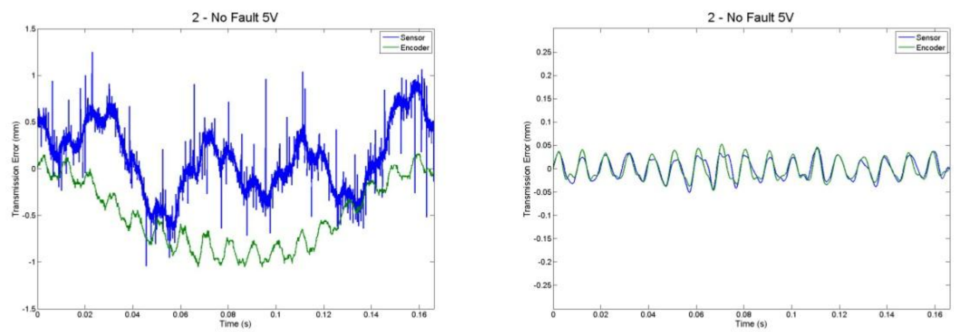

2 – No Fault 5V

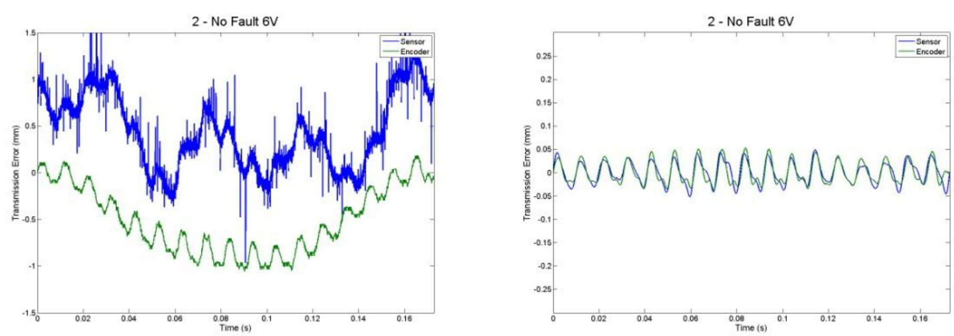

2 – No Fault 6V

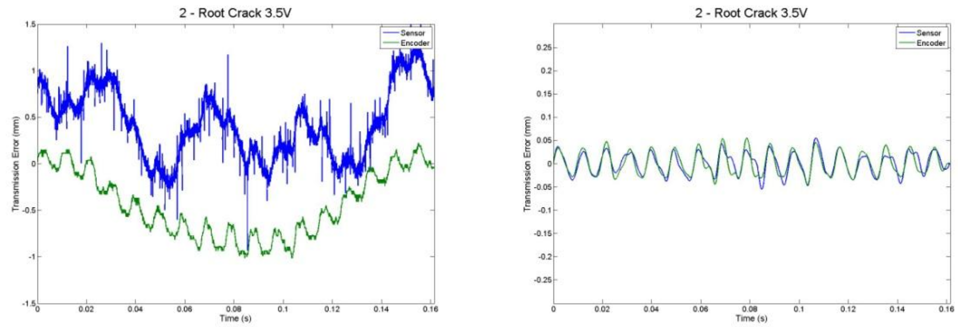

2 – Root Crack 3.5V

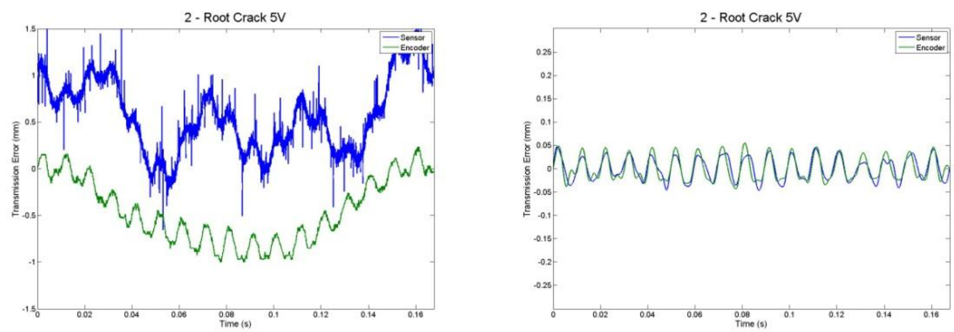

2 – Root Crack 5V

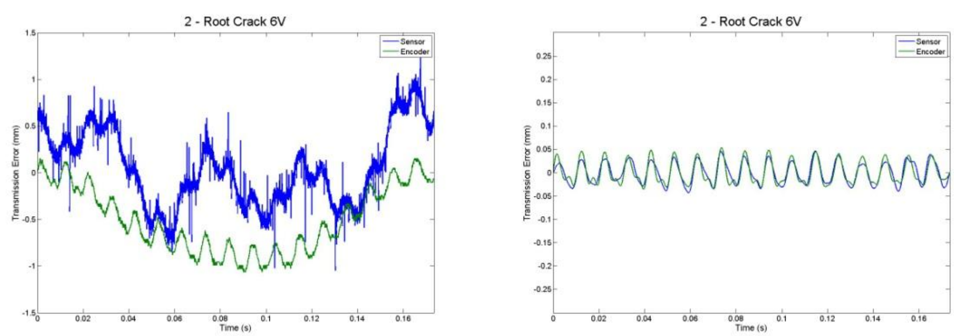

2 – Root Crack 6V

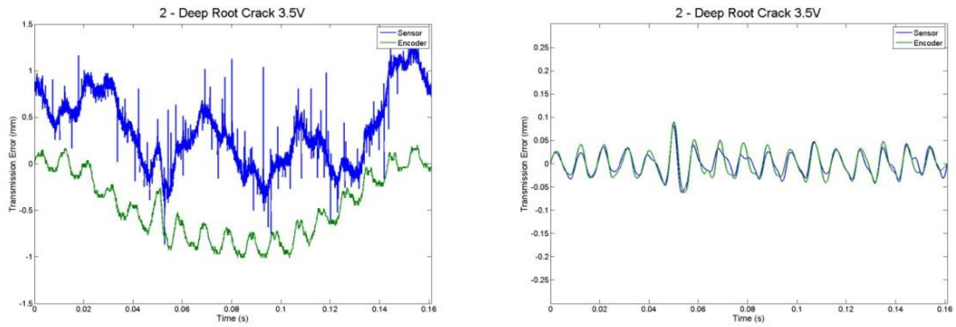

2 – Deep Root Crack 3.5V

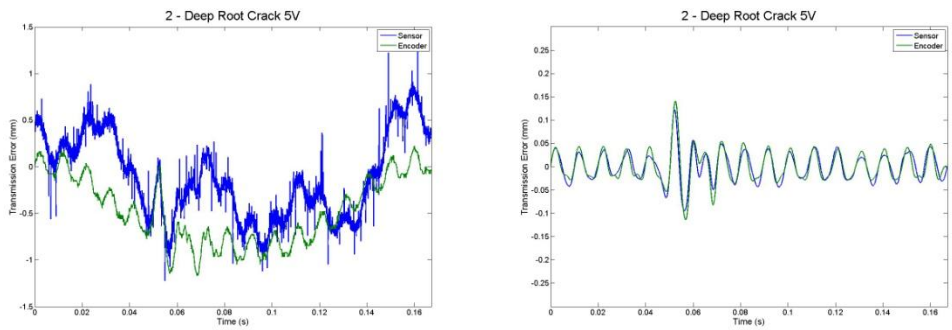

2 – Deep Root Crack 5V Early

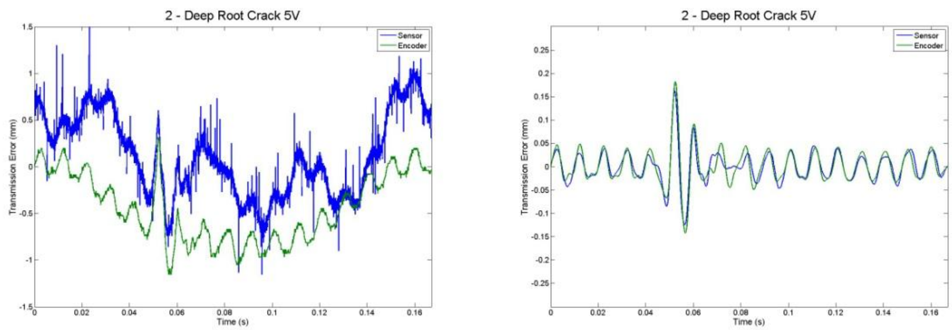

2 – Deep Root Crack 5V Late

Appendix C
Matlab Code

Final_extract_1() is the main function used to calculate and quantify Transmission Error. The target filename is the only necessary input, and it returns an array of characteristic features extracted from the filtered TE. This code was called by a script which would generate sequential filenames based on a root, and write results to a text file (which were imported into Excel).

………

```
function [file_output] = final_extract_1(dfile)
% dfile = 'No_Fault_010.lvm';
A = getdata(dfile);        % runs function to obtain the position data from
filename
B = normal(A);                   % normalize sensor data
in_rad = 50.8;                   % define pitch radii (mm)
out_rad = 50.8;

 % calculate sensor position
[linear_signal sawtooth_signal] = linear_pos2(B,in_rad,out_rad,200000);

% subtract shaft positions (raw TE)
[C sens_rel_pos] = subtract_pos2(sawtooth_signal);

 % find the unique starting index
initpos = zero_degrees(sawtooth_signal(:,1));

% find the finishing index (10 revolutions in this case)
[start finish] = encoder_pulse(A(:,5),initpos,3600);

% trim the relative error to 10 revolutions
sens_rel_pos_cut = sens_rel_pos(start:finish);
% filter sensor TE
sens_high_speed_error = moving_average(120,sens_rel_pos_cut);
sens_low_speed_error = moving_average(200,sens_rel_pos_cut);
sens_error = sens_high_speed_error - sens_low_speed_error;
```

```
% calculate encoder position for each shaft
input_enc_pos_long = encoder_position(A(:,5),1,finish+100);
output_enc_pos_long = encoder_position(A(:,6),1,finish+100);

% trim encoder position and calculate raw TE
input_enc_pos = input_enc_pos_long(start:finish);
output_enc_pos = output_enc_pos_long(start:finish);
enc_rel_pos = input_enc_pos - output_enc_pos - (input_enc_pos(1) -
output_enc_pos(1));

% filter encoder TE
b1 = moving_average(120,enc_rel_pos');
b2 = moving_average(200,enc_rel_pos');
enc_error = b1-b2;

% commented out section used to generate figures found in Section 5.4 and
Appendix B
% figure(14)
% set(axes,'FontSize',14)
% plot(0.00002:0.00002:length(sens_rel_pos_cut)*0.00002,sens_rel_pos_cut,
0.00002:0.00002:length(enc_rel_pos)*0.00002,enc_rel_pos,'LineWidth',2)
% ylim([-1.5 1.5])
% xlim([0 length(sens_error)*0.00002])
%
% % title(dfile(1:length(dfile)-8),'FontSize',24)
% title('No Fault 3.5V','FontSize',24)
% xlabel('Time (s)','FontSize',16)
% ylabel('Transmission Error (mm)','FontSize',16)
% legend('Sensor','Encoder')

% calculate characteristic features for sensor TE
m1_sens = max(sens_error);
m2_sens = min(sens_error);
rms_sens = norm(sens_error)/sqrt(length(sens_error));
mean1_sens = mean(sens_error);
kurt_sens = kurtosis(sens_error);

if abs(m1_sens) > abs(m2_sens)
```

```
    crest_sens = abs(m1_sens)/rms_sens;
else
    crest_sens = abs(m2_sens)/rms_sens;
end

% calculate characteristic features for encoder TE
m1_enc = max(enc_error);
m2_enc = min(enc_error);
rms_enc = norm(enc_error)/sqrt(length(enc_error));
mean1_enc = mean(enc_error);
kurt_enc = kurtosis(enc_error);

if abs(m1_enc) > abs(m2_enc)
    crest_enc = abs(m1_enc)/rms_enc;
else
    crest_enc = abs(m2_enc)/rms_enc;
end

% generate output array of extracted features (to be written in text file)
file_output = [rms_sens mean1_sens kurt_sens crest_sens rms_enc mean1_enc
kurt_enc crest_enc];
```

References

1 Mechefske, CK, 'Machine Condition Monitoring and Fault Diagnosis', Vibration and Shock Handbook, Edited by Clarence W. de Silva, CRC Press, Taylor and Francis Group, Boca Raton, Florida, USA, Chapter 25, pp 25-1 to 25-35, 2005.

2 Watson, H.J., 'Modern Gear Production', Pergamon of Canada Ltd., 207 Queen's Quay West, Toronto, Ontario, Canada Chapter 1, 16, 17 1970.

3 Affonso, Luiz Octávio Amaral, 'Machinery Failure Analysis Handbook - Sustain Your Operations and Maximize Uptime' (pp. 219-227). Gulf Publishing Company.

4 Smith, J.D., 'Gear Noise and Vibration', Marcel Dekker Inc, New York, USA, 1999.

5 Harris, S.L., ''Dynamic loads on the teeth of spur gears.' Proc.Inst. Mech. Eng., Vol 172, 1958, pp 87-112.

6 Cowan et al., 'Modern Tribology Handbook, Volumes I & II', CRC Press 2001

7 Yardley, E.D., 'The Use of Ferrography and Spectrographic Oil Analysis to Monitor the Performance of Three 90 kW Gearboxes', 4th International Tribology Conference, Paisley, Vol 56, pp 213-226, April 1979.

8 Endo, H; Randall, R B; Gosselin, C, 'Differential Diagnosis of Spall versus Cracks in the Gear Tooth Fillet Region', Journal of Failure Analysis and Prevention. Vol. 4, no. 5, pp. 63-71. Oct. 2004

9 Pallàs-Areny, Ramon; Webster, John G., 'Sensors and Signal Conditioning (2nd Edition)'. (pp. 433-445). John Wiley & Sons.

10 Sweeney, P.J. and Randall, R.B., 'Gear transmission error measurement using phase demodulation'. Proc. Inst. Mech. Eng., Vol 210C, 1996, pp 201-213.

11 Du, S, Randall, R. B, 'Encoder error analysis in gear transmission error measurement.', Proceedings of the Institution of Mechanical Engineers. Part C, Journal of Mechanical Engineering Science, vol. 212, no. C4, pp. 277-85, 1998

12 Remond, D, 'Practical performances of high-speed measurement of gear transmission error or torsional vibrations with optical encoders', Measurement Science & Technology, vol.9, no.3, pp.347-353, March 1998

13 Smith, J.D., 'Accuracy of small encoders for gear transmission errors', Proceedings of the Institution of Mechanical Engineers. Part C, Journal of Mechanical Engineering Science, vol. 215, no. C8, pp. 995-8, 2001

14 Obtained on Feb 18/2010 from http://www.electrical-res.com/earth-magnetic-flux-density_2221/

15 Smith, J.D. 'Gears and their Vibrations', Marcel Dekker Inc, New York, USA, pp. 55 1983.